

COMPUTATIONAL HYPERGRAPH DISCOVERY, A GAUSSIAN PROCESS FRAMEWORK FOR CONNECTING THE DOTS

THÉO BOURDAIS[†], PAU BATLLE[†], XIANJIN YANG[†], RICARDO BAPTISTA[†],
NICOLAS ROUQUETTE* AND HOUMAN OWHADI[†]

ABSTRACT. Most scientific challenges can be framed into one of the following three levels of complexity of function approximation. **Type 1:** Approximate an unknown function given input/output data. **Type 2:** Consider a collection of variables and functions, some of which are unknown, indexed by the nodes and hyperedges of a hypergraph (a generalized graph where edges can connect more than two vertices). Given partial observations of the variables of the hypergraph (satisfying the functional dependencies imposed by its structure), approximate all the unobserved variables and unknown functions. **Type 3:** Expanding on Type 2, if the hypergraph structure itself is unknown, use partial observations of the variables of the hypergraph to discover its structure and approximate its unknown functions. While most Computational Science and Engineering and Scientific Machine Learning challenges can be framed as Type 1 and Type 2 problems, many scientific problems can only be categorized as Type 3. Despite their prevalence, these Type 3 challenges have been largely overlooked due to their inherent complexity. Although Gaussian Process (GP) methods are sometimes perceived as well-founded but old technology limited to Type 1 curve fitting, their scope has recently been expanded to Type 2 problems. In this paper, we introduce an interpretable GP framework for Type 3 problems, targeting the data-driven discovery and completion of computational hypergraphs. Our approach is based on a kernel generalization of (1) Row Echelon Form reduction from linear systems to nonlinear ones and (2) variance-based analysis. Here, variables are linked via GPs, and those contributing to the highest data variance unveil the hypergraph’s structure. We illustrate the scope and efficiency of the proposed approach with applications to (algebraic) equation discovery, network discovery (gene pathways, chemical, and mechanical), and raw data analysis.

1. Introduction.

1.1. The three levels of complexity of function approximation. Alfred North Whitehead stated in 1911: "Civilization advances by extending the number of important operations we can perform without thinking about them." The automation of arithmetic and calculus through the introduction of calculators and computers serves as a testament to such transformative shifts. In line with this perspective, the resolution of most scientific challenges could be facilitated by automating the resolution of the following three levels of increasing complexity of function approximation (see Fig. 1).

[†]Department of Computing and Mathematical Sciences, California Institute of Technology, Pasadena, CA 91125, USA

*Jet Propulsion Laboratory, California Institute of Technology, Pasadena, CA 91109, USA

E-mail addresses: tbourdai@caltech.edu, pau@caltech.edu, yxjmath@caltech.edu, rsb@caltech.edu, nicolas.f.rouquette@jpl.nasa.gov, owhadi@caltech.edu

- **Type 1 (Regression):** Approximate an unknown function given (possibly noisy) input/output data.
- **Type 2 (Hypergraph Completion):** Consider a collection of variables and functions, some of which are unknown, indexed by the nodes and hyperedges of a hypergraph (a generalized graph where edges can connect more than two vertices). Given partial observations of the variables of the hypergraph (satisfying the functional dependencies imposed by its structure), approximate all the unobserved variables and unknown functions.
- **Type 3 (Hypergraph Discovery):** Expanding on Type 2, if the hypergraph structure itself is unknown, use partial observations (of subsets of the variables of the hypergraph) to discover its structure (the hyperedges and possibly the missing vertices) and then approximate its unknown functions and unobserved variables.

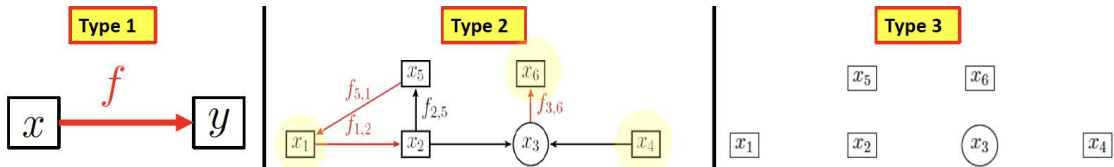


FIGURE 1. The three levels of complexity of function approximation.

The scope of these problems is immense. Numerical approximation, Supervised Learning, and Operator Learning can all be formulated as type 1 problems (possibly with functional inputs/outputs spaces). Type 2 problems include (see Fig. 4) solving and learning (possibly stochastic) ordinary or partial differential equations, Deep Learning, dimension reduction, reduced-ordered modeling, system identification, closure modeling, etc. The scope of Type 3 problems extends well beyond Type 2 problems and includes applications involving model/equation/network discovery and reasoning with raw data. While most problems in Computational Sciences and Engineering (CSE) and Scientific Machine Learning (SciML) can be framed as Type 1 and Type 2 challenges, many problems in science can only be categorized as Type 3 problems. Despite their prevalence, these Type 3 challenges have been largely overlooked due to their inherent complexity.

Causal inference methods and probabilistic graphs, as discussed in Section 3.3, and sparse regression methods [11, 4], offer potential avenues for addressing Type 3 problems. However, it is important to note that their application to these problems necessitates additional assumptions. Causal inference models, for instance, typically assume randomized data and some level of access to the data generation process or its underlying distributions. We emphasize that our proposed approach does not seek to replace causal inference methods but rather seeks to encode a different type of information into the structure of the graph, i.e., the functional dependencies between variables (see Sec. 3.3 for a more detailed discussion). Sparse regression methods, on the other hand, rely on the assumption that functional dependencies have a sparse representation within a known basis. In this paper, we do not impose these assumptions, and thus, these particular techniques may not be applicable.

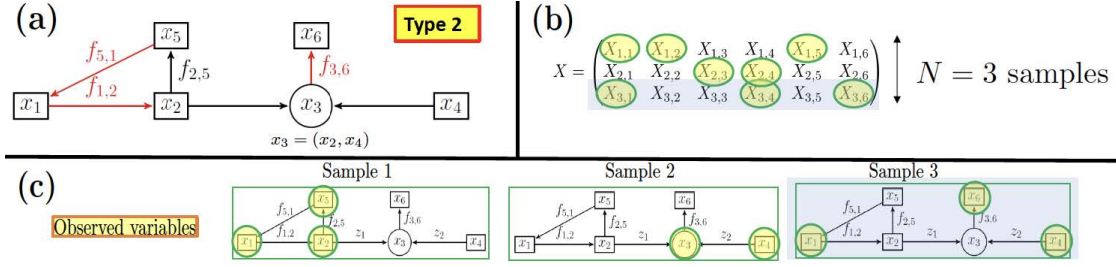


FIGURE 2. Formal description of Type 2 problems.

1.2. Type 2 problems: Formal description and GP-based Computational Graph Completion.

1.2.1. Formal description of Type 2 problems. Consider a computational graph (as illustrated in Fig. 2.(a)) where nodes represent variables and edges are directed and they represent functions. These functions may be known or unknown. In Fig. 2.(a), edges associated with unknown functions ($f_{5,1}$, $f_{1,2}$, $f_{3,6}$) are colored in red, and those associated with known functions ($f_{2,5}$) are colored in black. Round nodes are utilized to symbolize variables, which are derived from the concatenation of other variables (e.g, in Fig. 2.(a), $x_3 = (x_2, x_4)$). Therefore, the underlying graph is, in fact, a hypergraph where functions may map groups of variables to other groups of variables, and we use round nodes to illustrate the grouping step. Given partial observations derived from N samples of the graph's variables, we introduce a problem, termed a Type 2 problem, focused on approximating all unobserved variables and unknown functions. Using Fig. 2.(a)-(b) as an illustration we call a vector $(X_{s,1}, \dots, X_{s,6})$ a sample from the graph if its entries are variables satisfying the functional dependencies imposed by the structure of the graph (i.e., $X_{s,1} = f_{5,1}(X_{s,5})$, $X_{s,2} = f_{1,2}(X_{2,s})$, $X_{s,3} = (X_{s,2}, X_{s,4})$, $X_{s,5} = f_{s,5}(X_{s,s})$, and $X_{s,6} = f_{3,6}(X_{s,3})$). These samples can be seen as the rows of given matrix X illustrated in Fig. 2.(b) for $N = 3$. By partial observations, we mean that only a subset of the entries of each row may be observed, as illustrated in Fig. 2.(b)-(c). Note that a Type 2 problem combines a regression problem (approximating the unknown functions of the graph) with a matrix completion/data imputation problem (approximating the unobserved entries of the matrix X).

1.2.2. Reminder on Computational Graph Completion for Type 2 problems.

Although Gaussian Process (GP) methods are sometimes perceived as a well-founded but old technology limited to curve fitting (Type 1 problems), they have recently been generalized, beyond Type 1 problems [26, 27, 37, 35, 16, 17, 36, 3], to an interpretable framework (Computational Graph Completion or CGC [28]) for solving Type 2 problems [29, 5, 2, 6, 8, 18], all while maintaining the simple and transparent theoretical and computational guarantees of kernel/optimal recovery methods [22, 26].

Within the context of Sec. 1.2.1, the proposed GP solution to Type 2 problems is to simply replace unknown functions by GPs and compute their Maximum A Posteriori (MAP)/Maximum Likelihood Estimation (MLE) estimators given available data and constraints imposed by the structure of the graph. Taking into account the example depicted in Fig. 2, and substituting $f_{5,1}$, $f_{1,2}$, and $f_{3,6}$ with independent GPs, each with

kernels K , G , and Γ respectively, the objective of this MAP solution becomes minimizing $\|f_{5,1}\|_K^2 + \|f_{1,2}\|_G^2 + \|f_{3,6}\|_\Gamma^2$ (writing $\|f\|_K$ for the RKHS norm of f induced by the kernel K) subject to the constraints imposed by the data and the functional dependencies encoded into the structure of the graph.

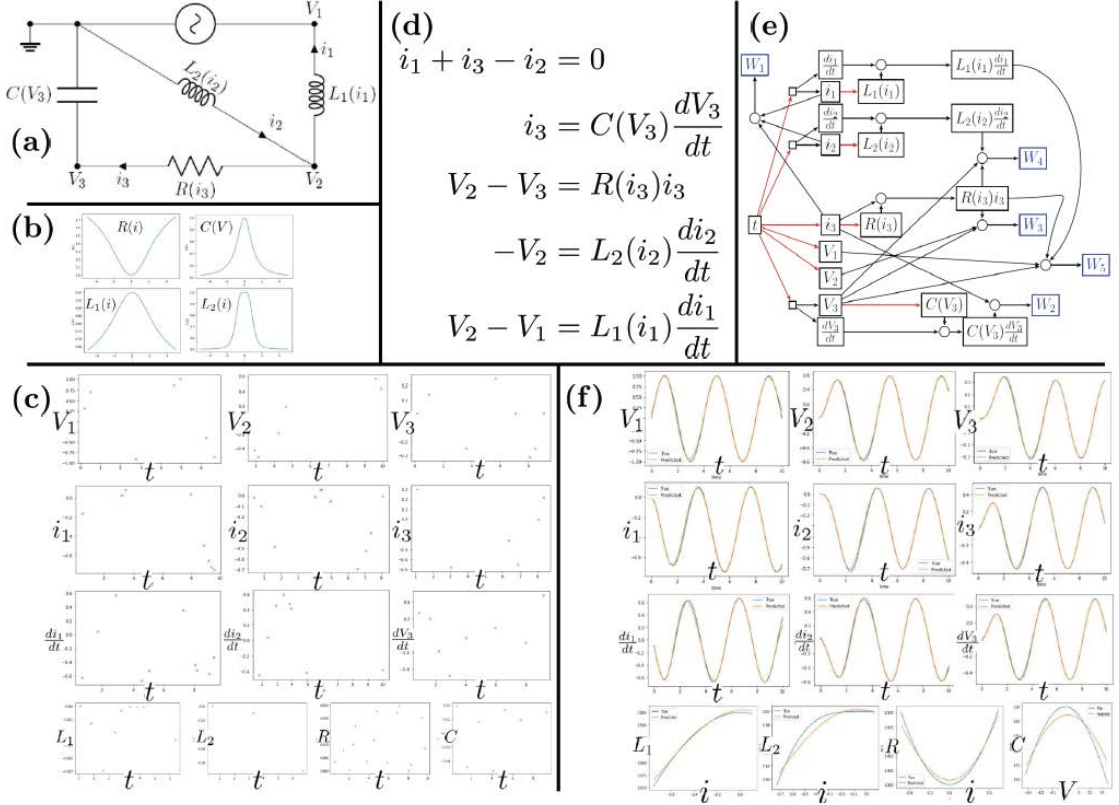


FIGURE 3. (a) Electric circuit. (b) Resistance, capacitance, and inductances are nonlinear functions of currents and voltages (c) Measurements. (d) Kirchhoff's circuit laws. (e) The computational graph with unknown functions represented as red edges. (f) Recovered functions.

1.2.3. A system identification example. In order to exemplify Computational Graphical Completion (CGC), consider the system identification problem depicted in Fig. 3, sourced from [28]. Our objective is to identify a nonlinear electric circuit, as illustrated in Fig. 3.(a), from scarce measurement data. The nonlinearity of the circuit emanates from the resistance, capacitance, and inductances, which are nonlinear functions of currents and voltages, as shown in Fig. 3.(b). Assuming these functions to be unknown, along with all currents and voltages as unknown time-dependent functions, we operate the circuit between times 0 and 10. Measurements of a subset of variables, representing the system's state, are taken at times $t_s = s/10$ for $s \in 0, \dots, 99$. Given these measurements, the challenge arises in approximating all unknown functions that define currents

and voltages as time functions, capacitance as a voltage function, and inductances and resistance as current functions. Fig. 3.(c) displays the available measurements, which are notably sparse, preventing us from reconstructing the underlying unknown functions independently. Thus, their interdependencies must be utilized for approximation. It is crucial to note that the system's state variables are interconnected through functional relations, as per Kirchoff's laws for this nonlinear electric circuit, illustrated in Fig.3.(d). These functional dependencies can be conceptualized as a computational graph, depicted in Fig.3.(e), where nodes represent variables and directed edges represent functions. Known functions are colored in black, unknown functions in red, and round nodes aggregate variables, meaning edges map groups of variables, forming a hypergraph. The CGC solution involves substituting the graph's unknown functions with Gaussian Processes (GPs), which may be independent or correlated, and then approximating the unknown functions with their Maximum A Posteriori (MAP) estimators, given the available data and the functional dependencies embedded in the graph's structure. Fig. 3.(f) showcases the true and recovered functions, demonstrating a notably accurate approximation despite the data's scarcity.

This simple example generalizes to an abstract framework detailed in [28]. This framework has a wide range of applications because most problems in CSE can also be formulated as completing computational graphs representing dependencies between functions and variables, and they can be solved in a similar manner by replacing unknown functions with GPs and by computing their MAP/EB estimator given the data. These problems include (see Fig. 4) solving and learning PDEs [5, 2, 6], learning SDEs [8], learning dynamical systems from partial observations [18], Deep Learning [29], etc. Although ANNs are oftentimes used to solve Type 1 problems, their training (the identification of unknown functions encoded into their layers) is a Type 2 problem as illustrated in Fig. 4 for a ResNet (see [29] for details on the proposed GP solution/regularization).

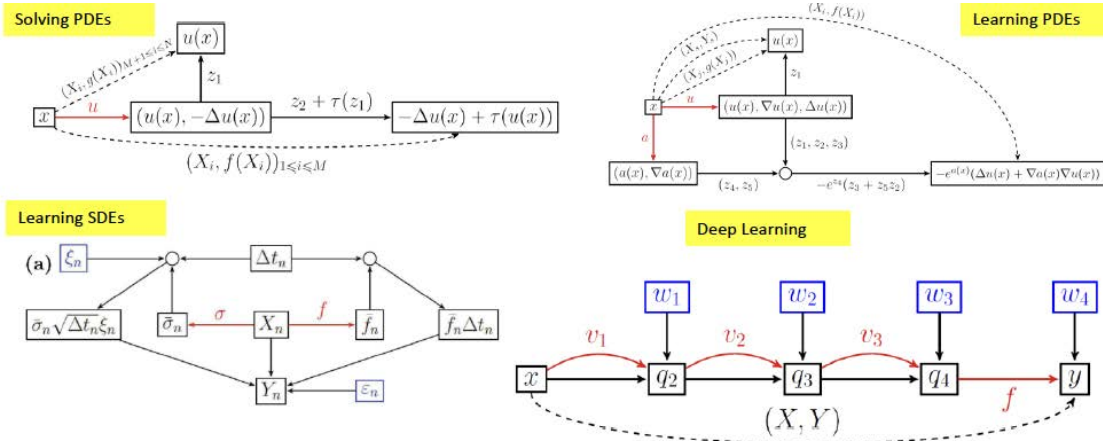


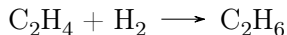
FIGURE 4. Examples of problems that can be solved as Type 2 problems.

1.3. Examples of Computational Hypergraph Discovery (Type 3) problems.

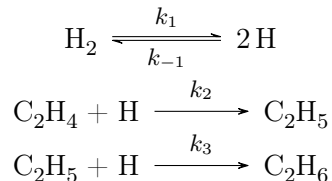
While most problems in Computer Science and Engineering can be framed and resolved

as computational graph or hypergraph completion tasks, some scientific challenges necessitate first uncovering the hypergraph’s structure before completing it. To illustrate the need for our proposed Computational Hypergraph Discovery framework, we will describe examples of these challenges, some of which are addressed in this paper.

1.3.1. Recovery of chemical reaction networks. One such problem is the recovery of chemical reaction networks from concentration snapshots. As an example consider the hydrogenation of ethylene (C_2H_4) into ethane (C_2H_6) (described in [19]). A proposed mechanism for this chemical reaction, represented by



is



The problem is that of recovering the underlying chemical reaction network from snapshots (illustrated in Fig. 5) of concentrations $[H_2]$, $[H]$, $[C_2H_4]$ and $[C_2H_5]$ and their time derivatives. $\frac{d[H_2]}{dt}$, $\frac{d[H]}{dt}$, $\frac{d[C_2H_4]}{dt}$ and $\frac{d[C_2H_5]}{dt}$.

1.3.2. Data analysis. Another problem is data analysis. As an example, consider the analysis of COVID-19 data from Google¹. Focus on a single country, France, to ensure consistency in the data and avoid considering cross-border variations that are not directly reflected in the data. Select 31 variables that describe the state of the country during the pandemic, spanning over 500 data points, with each data point corresponding to a single day. These variables are categorized as the following datasets:

- Epidemiology dataset: Includes quantities such as new infections, cumulative deaths, etc.
- Hospital dataset: Provides information on the number of admitted patients, patients in intensive care, etc.
- Vaccine dataset: Indicates the number of vaccinated individuals, etc.
- Policy dataset: Consists of indicators related to government responses, such as school closures or lockdown measures, etc.

Some of these variables are illustrated in Fig. 6. The problem is then to analyze this data and identify possible hidden functional relations between these variables.

1.3.3. Hidden algebraic equations. Another problem is equation discovery. As an example let w_1, w_2, w_3, w_4 and x_1, x_2 be six variables such that the w_i are i.i.d. $\mathcal{N}(0, 1)$ random variables, and x_1, x_2 satisfy $x_1 = w_1 w_2$ and $x_2 = w_2 \sin(w_4)$. Then, given $N = 1000$ observations of (samples from) those variables, consider the problem of discovering hidden functional relationships or dependencies between these variables (see Fig. 7.(a)).

¹The dataset can be accessed [here](#)

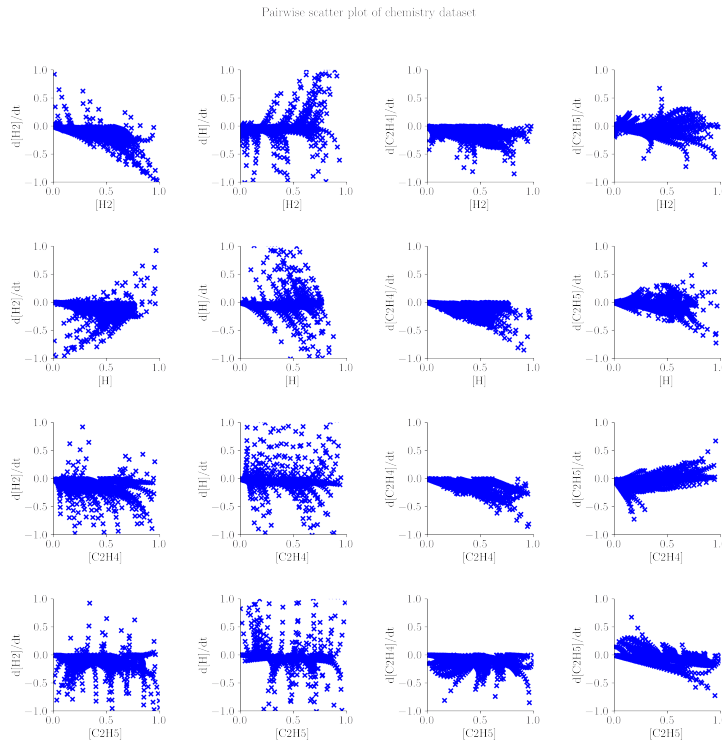


FIGURE 5. Pairwise scatter plot of the derivative and non-derivative variables of the chemistry problem

1.3.4. Computational Biology. An open problem in computational biology is to identify pathways and interactions between genes from their expression levels. One example stems from phosphorylated proteins and phospholipids in the human immune system T-cells presented in [34]. This dataset consists of 11 proteins and $N = 7446$ samples of their expressions. Fig. 7.(b) presents the (reference) causal dependencies found using experiments and structure learning algorithms for Bayesian networks, i.e., the directed acyclic graph identified in [34] from the cell-signaling data.

1.3.5. Land surface modeling. Another example (see Fig. 7.(c) from [10]) is the modeling of land surface interactions in weather prediction, and the problem is to discover possibly hidden functional dependencies between state variables for a finite number of snapshots of those variables.

1.3.6. Economic network analysis. Another example (see Fig. 7.(d) from [38]) is the recovery and analysis of economic networks, and the problem is to discover functional dependencies between the economic markers of different agents or companies, which is significant to systemic risk analysis.

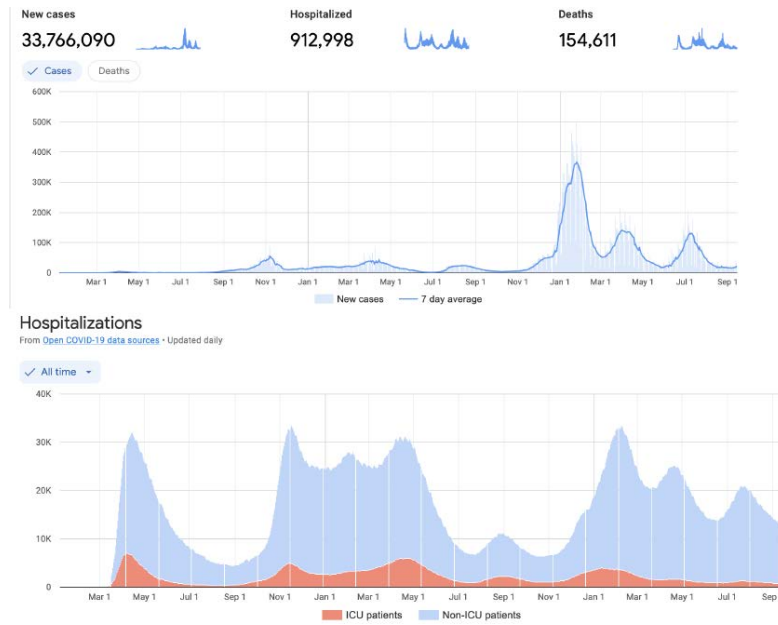


FIGURE 6. Google Covid-19 open data (France).

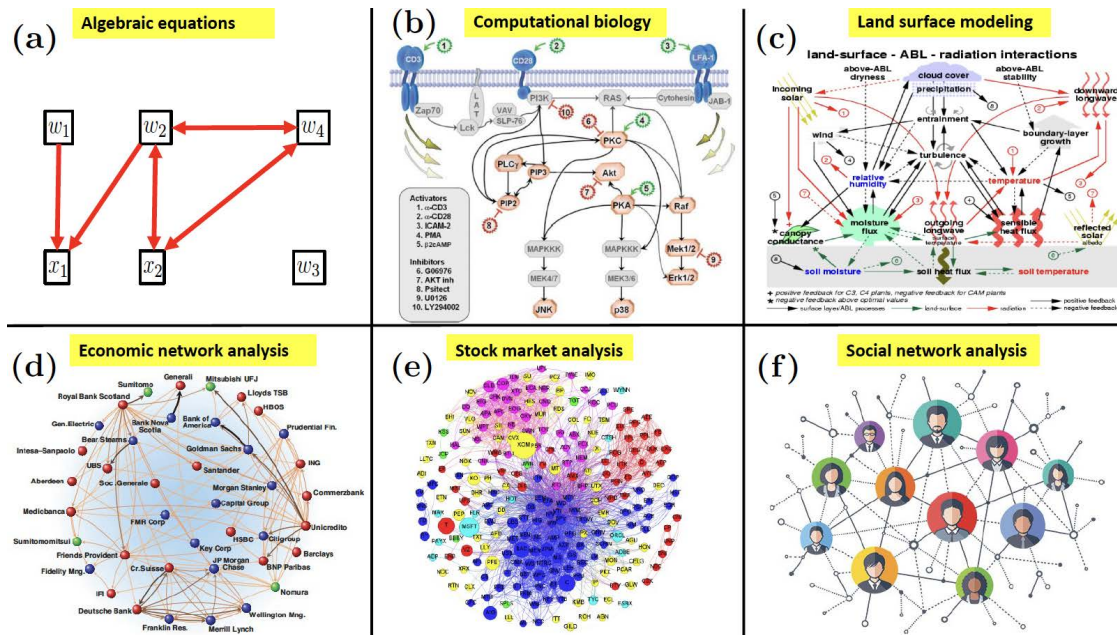


FIGURE 7. Examples of Computational Hypergraph Discovery problem

1.3.7. Graph analysis of the stock market. Another example (see Fig. 7.(e) from [44]) concerns a graph analysis of the stock market, and the problem is to discover functional dependencies between the price returns of different stocks.

1.3.8. Social network analysis. Another example (see Fig. 7.(f) from [14]) is social network analysis/discovery, and the problem is to discover functional dependencies between quantitative markers associated with each individual (a vector of numbers per individual) in situations where the connectivity of the network may be hidden.

1.4. Objectives, contributions, and structure of this paper. In this paper, we introduce an interpretable GP framework for Type 3 problems, targeting the data-driven discovery and completion of computational hypergraphs in the setting where the variables/nodes of the hypergraph are assumed to be known and its hyperedges/connectivity are unknown.

This work is organized as follows:

Sec. 2 presents a simplified overview of the proposed approach for Type 3 problems, with an application example, the Fermi-Pasta-Ulam-Tsingou (FPUT) problem.

Sec. 3 discusses the hardness of Type 3 problems (curse of combinatorial complexity, non-identifiability), proposes the well-posed formulation of such problems as a manifold learning problem, and reviews related causal inference approaches that could be employed for Type 3 problems under additional assumptions (access to the distributions of the underlying variables) which are not made here. In that sense, our method is different from all probabilistic approaches (targeting causal effects or conditional (in)dependencies).

Sec. 4 encapsulates the technical description of our method and presents the refinements needed to transform the simplified approach in Sec. 2 into a general-use algorithm. In particular, Sec. 4.1 shows that when the relations between variables are affine, then hypergraph discovery is equivalent to the Row Echelon Form reduction of the linear systems of equations encoded by the data. Sec. 4.2 presents a feature-map generalization of Row Echelon Form reduction from linear systems to nonlinear ones that can be represented by a given finite-dimensional feature-map given sufficient data. Sec. 4.3 presents a kernel-generalization of Row Echelon Form reduction encompassing arbitrarily complex functional dependencies between variables, low data regimes, regularization and generalization of free and dependent variables based on Kernel Mode Decomposition [30]. The proposed approach includes a kernel generalization of variance-based sensitivity analysis guiding the discovery of the structure of the hypergraph. Here, variables are linked via GPs, and those contributing to the highest data variance unveil the hypergraph's structure. This GP variance decomposition of the data leads to signal-to-noise and a Z-score that can be employed to determine whether a given variable can be approximated as a nonlinear function of a given number of other variables.

Sec. 5 presents two algorithms/pseudocodes summarizing the proposed approach whose main steps are as follows: (1) For each variable of the hypergraph, try to approximate its values as a sum of noise and a function of the values of other variables in a given set of ancestors. (2) If the signal-to-ratio exceeds a given threshold, then iteratively remove variables that are least contributing to the signal until the signal-to-noise ratio drops a given threshold.

Sec. 6 provides a theoretical analysis of the signal-to-noise ratio which leads to a method for choosing the prior variance γ of the noise.

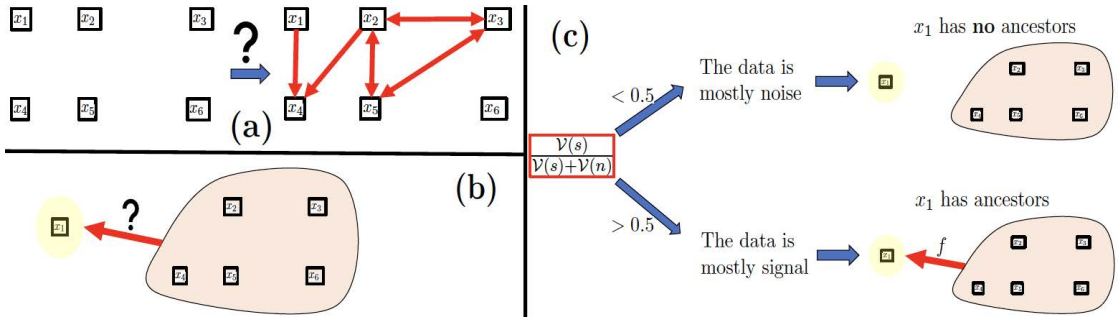


FIGURE 8. Ancestors identification in Type 3 problem.

Sec. 7 presents numerical experiments illustrating the scope and efficiency of the proposed approach. These include (algebraic) equation discovery, network discovery (gene pathways, chemical, and mechanical), and raw data analysis (Covid-19 open data).

2. Overview of the proposed approach for Type 3 problems

In this section, we present an algorithmic overview of the proposed approach for Type 3 problems. For ease of presentation, we consider the simple setting of Fig. 8.(a) where we are given N samples on the variables x_1, \dots, x_6 . After measurements/collection, these variables are normalized to have zero mean and unit variance. Our objective is to uncover the underlying dependencies between them. The code for this algorithm and its application to various examples are available for download (and as an installable python library/package) in the [Github repository of the paper](#).

2.1. A signal-to-noise ratio to decide whether or not a node has ancestors.

Our algorithm's core concept is the identification of ancestors for each node in the graph. Let's explore this idea in the context of a specific node, say x_1 , as depicted in Fig. 8.(b). Determining whether x_1 has ancestors is akin to asking if x_1 can be expressed as a function of x_2, x_3, \dots, x_6 . In other words, can we find a function f (living in a pre-specified space of functions that could be of controlled regularity) such that:

$$x_1 \approx f(x_2, \dots, x_6) \quad (2.1)$$

To answer this question we regress f with a centered GP $\xi \sim \mathcal{N}(0, \Gamma)$ whose covariance function Γ is an additive kernel of the form

$$\Gamma = K_s + \gamma\delta(x - y), \quad (2.2)$$

where K_s is a smoothing kernel, $\gamma > 0$ and $\delta(x - y)$ is the white noise covariance operator. This is equivalent to assuming the GP ξ to be the sum of two independent GPs, i.e., $\xi = \xi_s + \xi_n$ where $\xi_s \sim \mathcal{N}(0, K_s)$ is a smoothing/signal GP and $\xi_n \sim \mathcal{N}(0, \gamma\delta(x - y))$ is a noise GP. Writing \mathcal{H}_{K_s} for the RKHS induced by the kernel K , this is also equivalent to approximating f with a minimizer of

$$\inf_{f \in \mathcal{H}_K} \|f\|_{K_s}^2 + \frac{1}{\gamma} \|f(X) - Y\|_{\mathbb{R}^N}^2, \quad (2.3)$$

where $\|\cdot\|_{\mathbb{R}^N}^2$ is the Euclidean norm on \mathbb{R}^N , X is the input data on f obtained as an N -vector whose entries X_i are the samples on x_2, \dots, x_6 , Y is the output data on f obtained as an N -vector whose entries are obtained from the samples on x_1 , and $f(X)$ is a N -vector whose entries are the $f(X_i)$. At the minimum

$$\mathcal{V}(s) := \|f\|_{K_s}^2 \quad (2.4)$$

quantifies the data variance explained by the signal GP ξ_s and

$$\mathcal{V}(n) := \frac{1}{\gamma} \|f(X) - Y\|_{\mathbb{R}^N}^2 \quad (2.5)$$

quantifies the data variance explained by the noise GP ξ_n [30]. This allows us to define the signal-to-noise ratio

$$\frac{\mathcal{V}(s)}{\mathcal{V}(s) + \mathcal{V}(n)} \in [0, 1]. \quad (2.6)$$

If $\frac{\mathcal{V}(s)}{\mathcal{V}(s) + \mathcal{V}(n)} < 0.5^2$, then, as illustrated in Fig. 8.(c), we deduce that x_1 has no ancestors, i.e., x_1 cannot be approximated as function of x_2, \dots, x_6 . Conversely if $\frac{\mathcal{V}(s)}{\mathcal{V}(s) + \mathcal{V}(n)} > 0.5$, then, we deduce that x_1 has ancestors, i.e., x_1 can be approximated as function of x_2, \dots, x_6 .

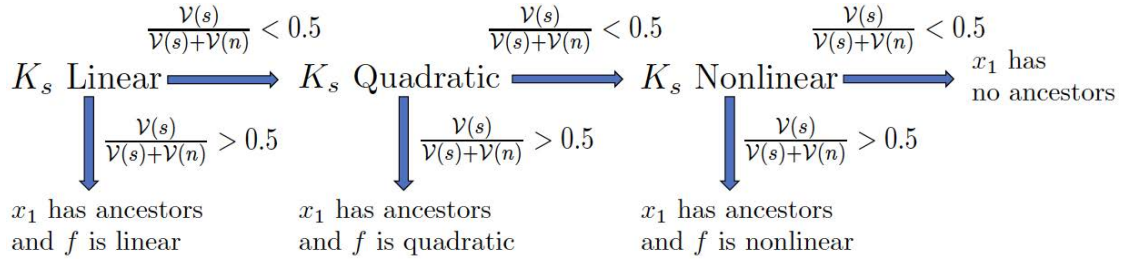


FIGURE 9. Selecting the signal kernel K_s .

2.2. Selecting the signal kernel K_s . This process is repeated by selecting the kernel K_s to be linear ($K_s(x, x') = 1 + \beta_1 \sum_i x_i x'_i$), quadratic ($K_s(x, x') = 1 + \beta_1 \sum_i x_i x'_i + \beta_2 \sum_{i \leq j} x_i x_j x'_i x'_j$) or fully nonlinear³ to identify f as linear, quadratic, or nonlinear. In the case of a nonlinear kernel, we employ:

$$K_s(x, x') = 1 + \beta_1 \sum_i x_i x'_i + \beta_2 \sum_{i \leq j} x_i x_j x'_i x'_j + \beta_3 \prod_i (1 + k(x_i, x'_i)) \quad (2.7)$$

where k is a universal kernel, such as a Gaussian or a Matérn kernel, with all parameters set to 1, and β_i assigned the default value 0.1. As illustrated in Fig. 9, we select K_s

²We will later present a version with a more sophisticated threshold method, but we keep the 0.5 threshold in this example for simplicity.

³By fully nonlinear, we mean not linear and not quadratic. We also call such kernels interpolatory because we select them as having an infinite-dimensional feature map. These kernels are also known as universal kernels. Abusing language, we may also call a kernel interpolatory when the number of data points is smaller than the dimension of the feature map.

as the first kernel that surpasses a signal-to-noise ratio of 0.5. If no kernel reaches this threshold, we conclude that x_1 lacks ancestors.

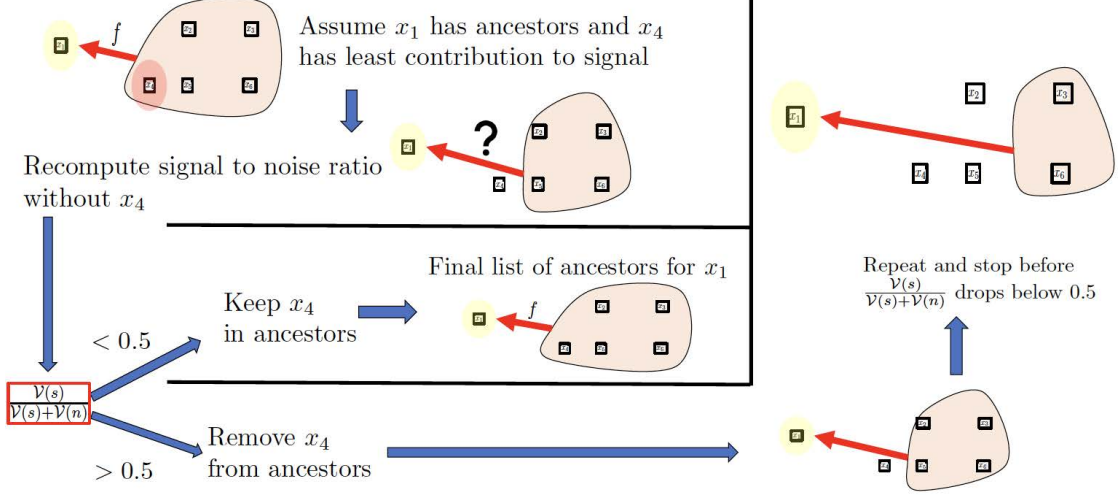


FIGURE 10. Pruning ancestors based on signal-to-noise ratio.

2.3. Pruning ancestors based on signal-to-noise ratio. Once we establish that x_1 has ancestors, the next step is to prune its set of ancestors iteratively. We remove nodes with the least contribution to the signal-to-noise ratio and stop before that ratio drops below 0.5 as illustrated in Fig. 10. To describe this, assume that K_s is as in (2.7). Then K_s is an additive kernel that can be decomposed into two parts:

$$K_s = K_1 + K_2, \quad (2.8)$$

where $K_1 = 1 + \beta_1 \sum_{i \neq 1,2} x_i x'_i + \beta_2 \sum_{i \leq j, i, j \neq 1,2} x_i x_j x'_i x'_j + \beta_3 \prod_{i \neq 1,2} (1 + k(x_i, x'_i))$ does not depend on x_2 and $K_2 = K_s - K_1$ depends on x_2 . This decomposition allows us to express f as the sum of two components:

$$f = f_1 + f_2, \quad (2.9)$$

where f_1 does not depend on x_2 , f_2 depends on x_2 and

$$(f_1, f_2) = \operatorname{argmin}_{(g_1, g_2) \in \mathcal{H}_{K_1} \times \mathcal{H}_{K_2}} \|g_1\|_{K_1}^2 + \|g_2\|_{K_2}^2. \quad (2.10)$$

Furthermore,

$$\|f\|_{K_s}^2 = \|f_1\|_{K_1}^2 + \|f_2\|_{K_2}^2, \quad (2.11)$$

and $\frac{\|f_2\|_{K_1}^2}{\|f\|_{K_s}^2} \in [0, 1]$ quantifies the contribution of x_2 to the signal data variance.

Following the procedure illustrated in Fig. 10, if, for example, x_4 is found to have the least contribution to the signal data variance, we recompute the signal-to-noise ratio without x_4 in the set of ancestors for x_1 . If that ratio is below 0.5, we do not remove x_4 from the list of ancestors, and x_2, x_3, x_4, x_5, x_6 is the final set of ancestors of x_1 . If this ratio remains above 0.5, we proceed with the removal. This iterative process continues,

and we stop before the signal-to-noise ratio drops below 0.5 to identify the final list of ancestors of x_1 .

2.4. Algorithm Overview: An Informal Summary. In this section, we provide an accessible overview of our algorithm’s key components, which are further detailed in Algorithms 1 and 2 in Section 5. Our method focuses on determining the edges within a hypergraph. To achieve this, we consider each node individually, finding its ancestors and establishing edges from these ancestors to the node in question. While we present the algorithm for a single node, it can be applied iteratively to all nodes within the graph.

Algorithm for finding the ancestors of a node:

- (1) **Initialization:** We start by assuming that all other nodes are potential ancestors of the current node.
- (2) **Selecting a Kernel:** We choose a kernel function, such as linear, quadratic, or fully nonlinear kernels (refer to Example 4.4). The kernel selection process is analogous to the subsequent pruning steps, involving the determination of a parameter γ , regression analysis, and evaluation based on signal-to-noise ratios.
 - **Kernel Selection Method:** The choice of kernel follows a process similar to the subsequent pruning steps, including γ selection, regression analysis, and signal-to-noise ratio evaluation.
 - **Low Signal-to-Noise Ratio for All Kernels:** If the signal-to-noise ratio is insufficient for all possible kernels, the algorithm terminates, indicating that the node has no ancestors.
- (3) **Pruning Process:** While there are potential ancestors left to consider (details in Section 4.3.5):
 - (a) **Identify the Least Important Ancestor:** Ancestors are ranked based on their contribution to the signal (see Sec. 4.3.3).
 - (b) **Noise prior:** Determine the value of γ (see Section 6.2).
 - (c) **Regression Analysis:** Predict the node’s value using the current set of ancestors, excluding the least active one (i.e., the one contributing the least to the signal). We employ Kernel Ridge Regression with the selected kernel function and parameter γ (see Sec. 4.3.3 and 4.3.3).
 - (d) **Evaluate Removal:** Compute the regression signal-to-noise ratio (see Sec. 4.3.4 and 6):
 - **Low Signal-to-Noise Ratio:** If the signal-to-noise ratio falls below a certain threshold, terminate the algorithm and return the current set of ancestors (see Section 4.3.6).
 - **Adequate Signal-to-Noise Ratio:** If the signal-to-noise ratio is sufficient, remove the least active ancestor and continue the pruning process.

2.5. Refinements. Throughout this paper, the approach presented in this section is refined and generalized, as discussed in the following subsections.

2.5.1. Complexity Reduction with Kernel PCA Variant. To improve the efficiency of our approach, we introduce a variant of Kernel PCA [23]. This modification significantly reduces the computational complexity of our proposed method, making it

primarily dependent on the number of principal nonlinear components in the underlying kernel matrices rather than the number of data points. See Sec. 4.3.2.

2.5.2. Generalizing Descendants and Ancestors with Kernel Mode Decomposition. We extend the concept of descendants and ancestors to cover more complex functional dependencies between variables, including implicit ones. This generalization is achieved through a Kernel-based adaptation of Row Echelon Form Reduction, initially designed for affine systems, and leveraging the principles of Kernel Mode Decomposition [30]. See Sec. 4.3.3.

2.5.3. Parameter Selection. The choice of the parameter γ is a critical aspect of our proposed approach. We provide a structured approach for selecting γ based on the characteristics of the kernel matrix K_s . Specifically, when K_s is derived from a finite-dimensional feature map ψ , we employ the regression residual to determine γ as follows: $\gamma = \min_v \|v^T \psi(X) - Y\|_{\mathbb{R}^N}^2$. This process is detailed in Sec. 6.2.1. Alternatively, when K_s is a universal kernel, we select γ by maximizing the variance of the eigenvalue histogram of $\gamma(K_s(X, X) + \gamma I)^{-1}$ (see Sec. 6.2.2).

2.5.4. Ancestor pruning. The most efficient version of our proposed algorithm (Alg. 2) does not use a threshold of 0.5 on the signal-to-noise ratio to prune ancestors, but it rather employs an inflection point in the noise-to-signal ratio $\frac{\mathcal{V}(n)}{\mathcal{V}(s)+\mathcal{V}(n)}(q)$ as a function of the number q of ancestors (Fig. 12). To put it simply, after ordering the ancestors in decreasing contribution to the signal, the final number q of ancestors is determined as the maximizer of $\frac{\mathcal{V}(n)}{\mathcal{V}(s)+\mathcal{V}(n)}(q+1) - \frac{\mathcal{V}(n)}{\mathcal{V}(s)+\mathcal{V}(n)}(q)$. We illustrate this algorithm in the following section with an application to the recovery of a mechanical network.

2.6. The Fermi-Pasta-Ulam-Tsingou problem. The Fermi-Pasta-Ulam-Tsingou (FPUT) problem, delineated in [31], is a renowned dynamical system for exploring chaotic systems.

It comprises a set of N masses, with mass $j \in \{0, \dots, N-1\}$ having a position at equilibrium $p_j = jh$ with $h = 1/N$. Each mass is tethered to its two adjacent masses by a spring, and an additional force defined by a function $\alpha : \mathbb{R} \rightarrow \mathbb{R}$. The displacement of the mass x_j adheres to the equation:

$$\ddot{x}_j = \frac{c^2}{h^2}(x_{j+1} + x_{j-1} - 2x_j)(1 + \alpha(x_{j+1} - x_{j-1})) \quad (2.12)$$

Here, c^2 is a velocity depending on h and the strength of the springs. We set $c = 1$ and $N = 10$. Furthermore, we use fixed boundary conditions by adding two more masses, with $x_{-1} = x_N = 0$.

The selection of this model to illustrate our framework is driven by several aspects: its chaotic behavior, established and sparse equations, and the presence of linear/nonlinear equations contingent on the choice of α . We simulate the system with two different choices of α : a nonlinear case where $\alpha(x) = x^2$, and a linear case where $\alpha(x) = 0$. Snapshots of the system, encapsulating the position, velocity, and acceleration of each mass, are collected at various time points. A thousand of these snapshots serve as data for our graph discovery algorithm. We use the algorithm from the preceding section, refined

with the optimal noise parameter from Sec. 6, the Z-score test, and the signal-to-noise ratio inflection point to select ancestors.

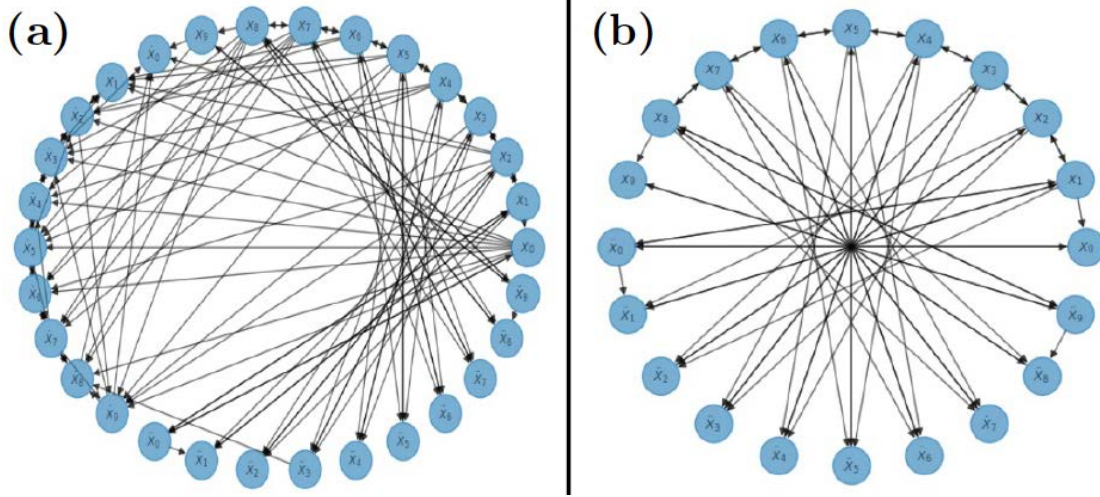


FIGURE 11. (a) Recovered full graph (b) Recovered subgraph for positions and accelerations.

The resultant graph, depicted in Fig.11.(a), showcases the graph discovery framework's aptitude in accurately identifying dependencies. Notably, speed information is accurately identified as non-essential and omitted from the ancestors of position and acceleration, underscoring the efficacy of the approach. The recovered dependencies are notably precise, especially considering the model's nonlinear nature. Fig.11.(b), which omits speed information for clarity, further elucidates the accurate recovery of dependencies. These dependencies are predominantly the simplest and most straightforward possible, with an exception for \ddot{x}_1 and \ddot{x}_8 , which have respective recovered ancestors $\{\ddot{x}_0, x_1, x_2\}$ and $\{\ddot{x}_9, x_8, x_7\}$, instead of $\{x_0, x_1, x_2\}$ and $\{x_9, x_8, x_7\}$. However, examining the equations for \ddot{x}_0 and \ddot{x}_9 reveals that they contain the information of (x_0, x_1) and (x_8, x_9) respectively, validating the recovered relationships as alternative formulations of the FPUT equations. It is crucial to note that multiple formulations of the same equations, with varying ancestor relationships, can generally exist.

While performing our experiments, a set threshold of 60% on the noise-to-signal ratio could be used to obtain the desired equations. However, this choice could be seen as arbitrary or guided by our knowledge of the true equations. However, the choice to retain or discard an ancestor becomes clear when examining the noise-to-signal ratio's evolution against the number of ancestors. In the graph discovery phase, every other node is initially deemed a potential ancestor for a specified node of interest. We then proceed to iteratively remove the node with the least signal contribution. The step resulting in the largest surge in the noise-to-signal ratio is inferred as one eliminating a crucial ancestor, thereby pinpointing the final ancestor set. In the context of the FPUT problem,

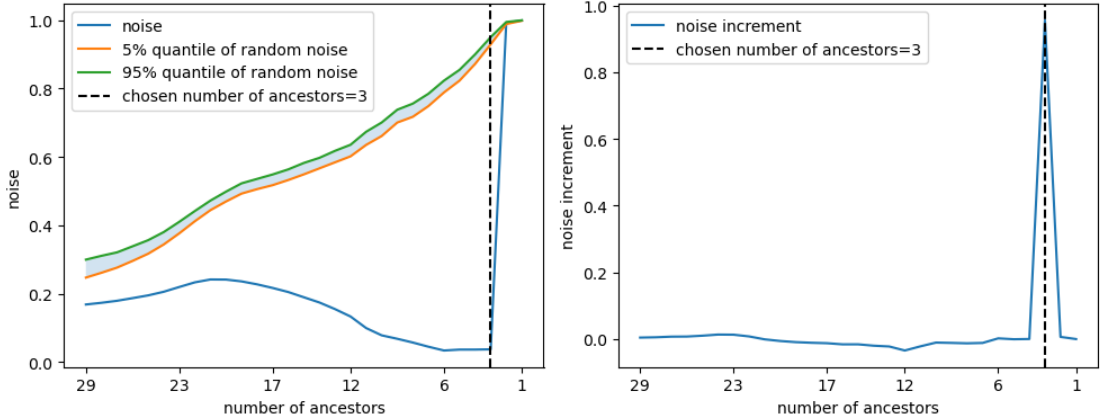


FIGURE 12. (a) Noise-to-signal ratio $\frac{\mathcal{V}(n)}{\mathcal{V}(s)+\mathcal{V}(n)}(q)$ as a function of the number q of proposed ancestors. We also plot the Z -test quantiles describe in Sec. 6.3 (in the absence of signal, the noise-to-signal ratio should fall within the shaded area with probability 0.9). (b) Noise-to-signal ratio increments $\frac{\mathcal{V}(n)}{\mathcal{V}(s)+\mathcal{V}(n)}(q) - \frac{\mathcal{V}(n)}{\mathcal{V}(s)+\mathcal{V}(n)}(q-1)$ as a function of the number q of ancestors. The x-axis represents the number q of proposed ancestors for \ddot{x}_7 . The removal of crucial ancestors, such as ancestor 3, results in the Noise-to-Signal Ratio saturating at a value of 1.0. This particular removal also leads to a significantly greater increase in the Noise-to-Signal Ratio compared to the removal of other ancestors.

we observed that, firstly, removing a node essential to the equation of interest causes the noise-to-signal ratio to markedly jump from approximately 25% to 99%. Additionally, we can analyze the increase in the noise-to-signal ratio during the removal process. Two representative trajectories illustrating this are presented in Fig. 12 and 13. Notably, in the final iteration where an essential node was removed, the increase in the noise-to-signal ratio is significantly higher compared to previous removals. This observation indicates that the process halted at the appropriate juncture, as the removal of this last node was not sanctioned. As shown in Fig. 13, while solely relying on a fixed threshold to decide when to cease the removals might prove challenging, evaluating the increments in noise-to-signal ratios offers a clear guideline for efficiently and reliably pruning ancestors.

3. Hardness and well-posed formulation of Type 3 problems

Having discussed why we should care about this problem, we will describe why the problem is challenging and why it can even be intractable if not formalized and approached properly.

3.1. Curse of combinatorial complexity. First, the problem suffers from the curse of combinatorial complexity in the sense that the number of hypergraphs associated with N nodes blows up rapidly with N . As an illustration, Fig. 14 shows some of

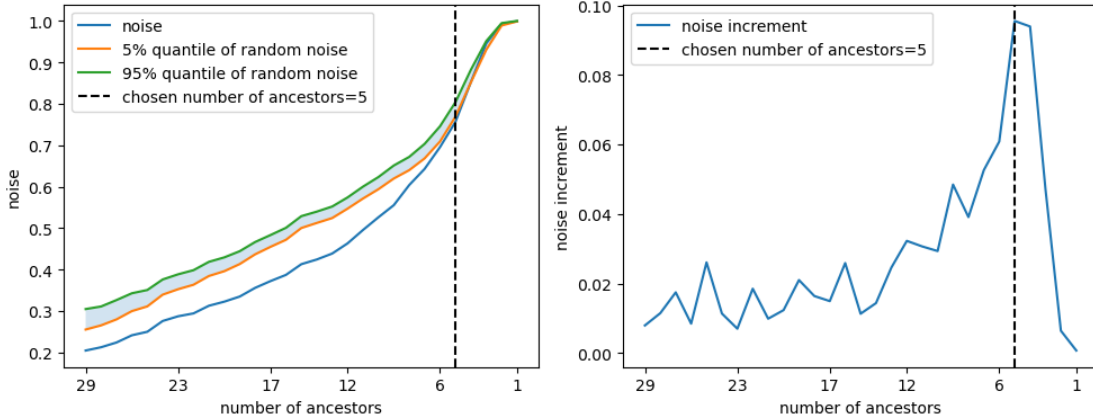


FIGURE 13. (a) Noise-to-Signal Ratio, denoted as $\frac{\mathcal{V}(n)}{\mathcal{V}(s)+\mathcal{V}(n)}(q)$, with respect to the number of proposed ancestors, represented by q . Additionally, we include a visualization of the quantiles derived from the Z -test, as described in Section 6.3. Notably, when there is no signal present, the noise-to-signal ratio is expected to fall within the shaded area with a probability of 0.9. (b) Increments in the Noise-to-Signal Ratio, defined as $\frac{\mathcal{V}(n)}{\mathcal{V}(s)+\mathcal{V}(n)}(q) - \frac{\mathcal{V}(n)}{\mathcal{V}(s)+\mathcal{V}(n)}(q-1)$, as a function of the number of ancestors, denoted as q . The horizontal axis represents the number of proposed ancestors for \dot{x}_0 . Determining an appropriate stopping point based solely on absolute noise-to-signal ratio levels can be challenging. In contrast, the increments in the noise-to-signal ratio clearly exhibit a discernible maximum, offering a practical point for decision-making.

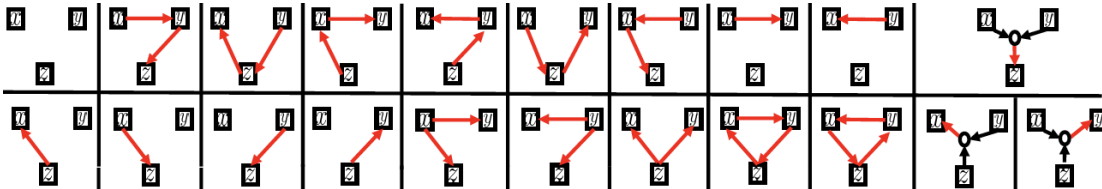


FIGURE 14. Computational Hypergraph Discovery with three variables

the hypergraphs associated with only three nodes. A lower bound on that number is the A003180 sequence, which answers the following question [20]: given N unlabeled vertices, how many different hypergraphs in total can be realized on them by counting the equivalent hypergraphs only once? For $N = 8$, this lower bound is $\approx 2.78 \times 10^{73}$.

3.2. Nonidentifiability and implicit dependencies. Secondly, it is important to note that, even with an infinite amount of data, the exact structure of the hypergraph might not be identifiable. To illustrate this point, let's consider a problem where we have N samples from a computational graph with variables x and y . The task is to

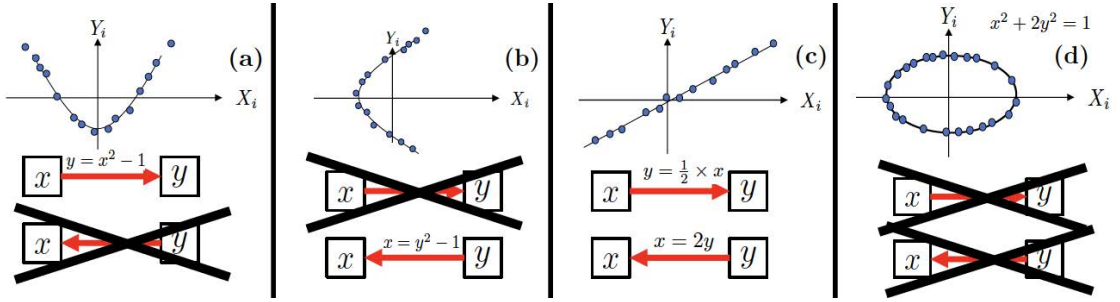


FIGURE 15. The structure of the hypergraph is identifiable in (a), (b), and non-identifiable in (c). The relationship between variables is implicit in (d).

determine the direction of functional dependency between x and y . Does it go from x to y (represented as $\square \xrightarrow{f} \square$), or from y to x (represented as $\square \xleftarrow{f} \square$)?

If we refer to Figure 15.(a), we can make a decision because y can only be expressed as a function of x . In contrast, if we examine Figure 15.(b), the decision is also straightforward because x can solely be written as a function of y . However, if the data mirrors the scenario in Figure 15.(c), it becomes challenging to decide as we can write both y as a function of x and x as a function of y . Further complicating matters is the possibility of implicit dependencies between variables. As illustrated in Figure 15.(d), there might be instances where neither y can be derived as a function of x , nor x can be represented as a function of y .

3.3. Causal inference and probabilistic graphs. The field of causal inference and probabilistic modeling, as outlined in [24, 15], seeks to address distinct graph learning problems by introducing auxiliary assumptions. Within noise and probabilistic models [43, 21], it is generally assumed that the data is randomized.

Causal inference methods broadly consist of two approaches: constraint and score-based methods. While constraint-based approaches are asymptotically consistent, they only learn the graph up to an equivalence class [42]. Instead, score-based methods resolve ambiguities in the graph's edges by evaluating the likelihood of the observed data for each graphical model. For instance, they may assign a higher evidence to $y \rightarrow x$ over $x \rightarrow y$ if the conditional distribution $x|y$ exhibits less complexity than $y|x$. The complexity of searching over all possible graphs, however, grows super-exponentially with the number of variables. Thus, it is often necessary to use approximate, but more tractable, search-based methods [7, 32] or alternative criteria based on sensitivity analysis [9]. For example, the preference could lean towards $y \rightarrow x$ rather than $x \rightarrow y$ if y demonstrates less sensitivity to errors or perturbations in x . In contrast, our proposed Gaussian Process method avoids the growth in complexity by performing a guided pruning process that assesses the contribution of each node to the signal, as detailed in Section 2.3. We also emphasize that our method is not limited to learning acyclic graph structures as it can identify feedback loops between variables.

Alternatively, methods for learning probabilistic undirected graphical models, also known as Markov networks, identify the graph structure by assuming the data is randomly drawn from some probability distribution [12]. In this case, edges in the graph (or

lack thereof) encode conditional dependencies between the nodes. A common approach learns the graph structure by modeling the data as being drawn from a multivariate Gaussian distribution with a sparse inverse covariance matrix, whose zero entries indicate pairwise conditional independencies [13]. Recently, this approach has been extended using models for non-Gaussian distributions, e.g., in [1, 33], as well as kernel-based conditional independence tests [46]. In this work, we learn functional dependencies rather than causality or probabilistic dependence. We emphasize that we also do not assume the data is randomized or impose strong assumptions, such as additive noise models, in the data-generating process.

We complete this subsection by comparing the hypergraph discovery framework to structure learning for Bayesian networks and structural equation models (SEM). Let $x \in \mathbb{R}^d$ be a random variable with probability density function p that follows the autoregressive factorization $p(x) = \prod_{i=1}^d p_i(x_i|x_1, \dots, x_{i-1})$ given a prescribed variable ordering. Structure learning for Bayesian networks aims to find the ancestors of variable x_i , often referred to as the set of parents $Pa(i) \subseteq \{1, \dots, i-1\}$, in the sense that $p_i(x_i|x_1, \dots, x_{i-1}) = p_i(x_i|x_{Pa(i)})$. Thus, the variable dependence of the conditional density p_i is identified by finding the parent set so that x_i is conditionally independent of all remaining preceding variables given its parents, i.e., $x_i \perp x_{1:i-1 \setminus Pa(i)} | x_{Pa(i)}$. Finding ancestors that satisfy this condition requires performing conditional independence tests, which are computationally expensive for general distributions [39]. Alternatively, SEMs assume that each variable x_i is drawn as a function of its ancestors with additive noise, i.e., $x_i = f(x_{Pa(i)}) + \epsilon_i$ for some function f and noise ϵ [32]. For Gaussian noise $\epsilon_i \sim \mathcal{N}(0, \sigma^2)$, each marginal conditional distribution in a Bayesian network is given by $p_i(x_i|x_{1:i-1}) \propto \exp(-\frac{1}{2\sigma^2} \|x_i - f(x_{1:i-1})\|^2)$. Thus, finding the parents for such a model by maximum likelihood estimation corresponds to finding the parents that minimize the expected mean-squared error $\|x_i - f(x_{Pa(i)})\|^2$. We will show that our approach minimizes a related objective in Section 4.3.3, without imposing the strong probabilistic assumptions that are required in SEMs and Bayesian Networks. We also observe that while the graph structure identified in Bayesian networks is influenced by the specific sequence in which variables are arranged (a concept exploited in numerical linear algebra [37, 35] where Schur complementation is equivalent to conditioning GPs and a carefully ordering leads to the accuracy of the Vecchia approximation $p_i(x_i|x_1, \dots, x_{i-1}) \approx p_i(x_i|x_{i-k}, \dots, x_{i-1})$ [45]), the graph recovered by our approach remains unaffected by any predetermined ordering of those variables.

3.4. Well-posed formulation of the problem. In this paper, we focus on a formulation of the problem that remains well-posed even when the data is not randomized, i.e., we formulate the problem as the following manifold learning/discovery problem.

Problem 1. *Let \mathcal{H} be a Reproducing Kernel Hilbert Space (RKHS) of functions mapping \mathbb{R}^d to \mathbb{R} . Let \mathcal{F} be a closed linear subspace of \mathcal{H} and let \mathcal{M} be a subset of \mathbb{R}^d such that $x \in \mathcal{M}$ if and only if $f(x) = 0$ for all $f \in \mathcal{F}$.*

Given the (possibly noisy and nonrandom) observation of N elements, X_1, \dots, X_N , of \mathcal{M} approximate \mathcal{M} .

To understand why problem 1 serves as the appropriate formulation for hypergraph discovery, consider a manifold $\mathcal{M} \subset \mathbb{R}^d$. Suppose this manifold can be represented by a

set of equations, expressed as a collection of functions $(f_k)_k$ satisfying $\forall x \in \mathcal{M}, f_k(x) = 0$. To keep the problem tractable, we assume a certain level of regularity for these functions, necessitating they belong to a RKHS \mathcal{H} , ensuring the applicability of kernel methods for our framework. Given that any linear combination of the f_k will also be evaluated to zero on \mathcal{M} , the relevant functions are those within the span of the f_k , forming a closed linear subspace of \mathcal{H} denoted as \mathcal{F} . The manifold \mathcal{M} can be subsequently represented by a graph or hypergraph (see Fig. 16.(a)), whose ambiguity can be resolved through a deliberate decision to classify some variables as free and others as dependent. This selection could be arbitrary, informed by expert knowledge, or derived from probabilistic models or sensitivity analysis.

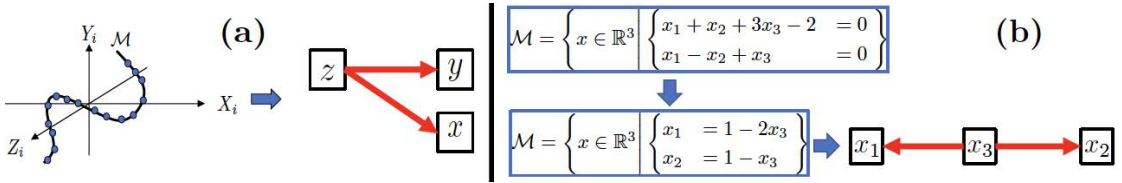


FIGURE 16. (a) CHD formulation as a manifold discovery problem and hypergraph representation (b) The hypergraph representation of an affine manifold is equivalent to its Row Echelon Form Reduction.

4. A Gaussian Process method for Type 3 problems

4.1. Affine case and Row Echelon Form Reduction. To describe the proposed solution to Problem 1, we start with a simple example. In this example \mathcal{H} is a space of affine functions f of the form

$$f(x) = v^T \psi(x) \text{ with } \psi(x) := \begin{pmatrix} 1 \\ x \end{pmatrix} \text{ and } v \in \mathbb{R}^{d+1}, \quad (4.1)$$

As a particular instantiation (see Fig. 16.(b)), we assume \mathcal{M} to be the manifold of \mathbb{R}^3 ($d = 3$) defined by the affine equations

$$\mathcal{M} = \left\{ x \in \mathbb{R}^3 \mid \begin{cases} x_1 + x_2 + 3x_3 - 2 = 0 \\ x_1 - x_2 + x_3 = 0 \end{cases} \right\}, \quad (4.2)$$

which is equivalent to selecting $\mathcal{F} = \text{span}\{f_1, f_2\}$ with $f_1(x) = x_1 + x_2 + 3x_3 - 2$ and $f_2(x) = x_1 - x_2 + x_3$ in the problem formulation 1.

Then, irrespective of how we recover the manifold from data, the hypergraph representation of that manifold is equivalent to the row echelon form reduction of the affine system, and this representation and this reduction require a possibly arbitrary choice of free and dependent variables. So, for instance, for the system (4.2), if we declare x_3 to be the free variables and x_1 and x_2 to be the dependent variables, then we can represent the manifold via the equations

$$\mathcal{M} = \left\{ x \in \mathbb{R}^3 \mid \begin{cases} x_1 = 1 - 2x_3 \\ x_2 = 1 - x_3 \end{cases} \right\}, \quad (4.3)$$

which have the hypergraph representation depicted in Fig. 16.(b).

Now, in the $N > d$ regime where the number of data points is larger than the number of variables, the manifold can simply be approximated via a variant of PCA. Take $f^* \in \mathcal{F}$, we have $f^*(x) = v^{*T}\psi(x)$ for a certain $v^* \in \mathbb{R}^{d+1}$. Then for $X_s \in \mathcal{M}$, $f^*(X_s) = \psi(X_s)^T v^* = 0$. Defining

$$C_N := \sum_{s=1}^N \psi(X_s)\psi(X_s)^T \quad (4.4)$$

we see that $f^*(X_s) = 0$ for all X_s is equivalent to $C_N v^* = 0$. Since $N > d$, we can thus identify \mathcal{F} exactly as $\{v^T \psi \text{ for } v \in \text{Ker}(C_N)\}$. We then obtain the manifold

$$\mathcal{M}_N = \{x \in \mathbb{R}^d \mid v^T \psi(x) = 0 \text{ for } v \in \text{Span}(v_{r+1}, \dots, v_{d+1})\} \quad (4.5)$$

where $\text{Span}(v_{r+1}, \dots, v_{d+1})$ is the zero-eigenspace of C_N . Here we write $\lambda_1 \geq \dots \geq \lambda_r > 0 = \lambda_{r+1} = \dots = \lambda_{d+1}$ for the eigenvalues of C_N (in decreasing order), and v_1, \dots, v_{d+1} for the corresponding eigenvectors ($C_N v_i = \lambda_i v_i$). The proposed approach extends to the noisy case (when the data points are perturbations of elements of the manifold) by simply replacing the zero-eigenspace of the covariance matrix by the linear span of the eigenvectors associated with eigenvalues that are smaller than some threshold $\epsilon > 0$, i.e., by approximating \mathcal{M} with (4.5) where r is such that $\lambda_1 \geq \dots \geq \lambda_r \geq \epsilon > \lambda_{r+1} \geq \dots \geq \lambda_{d+1}$. In this affine setting (4.5) allows us to estimate \mathcal{M} directly without RKHS norm minimization/regularization as discussed in Sec. 2 because linear regression does not require regularization in the sufficiently large data regime. Furthermore the process of pruning ancestors (also discussed in Sec. 2) can be replaced by that of identifying sparse elements $v \in \text{Span}(v_{r+1}, \dots, v_{d+1})$ such that $v_i = 1$.

4.2. Feature map generalization. This simple approach can be generalized by generalizing the underlying feature map ψ used to define the space of functions (writing d_S for the dimension of the range of ψ)

$$\mathcal{H} = \{f(x) = v^T \psi(x) \mid v \in \mathbb{R}^{d_S}\}. \quad (4.6)$$

For instance, if we use the feature map

$$\psi(x) := (1, \dots, x_i, \dots, x_i x_j, \dots)^T \quad (4.7)$$

then \mathcal{H} becomes a space of quadratic polynomials on \mathbb{R}^d , i.e.,

$$\mathcal{H} = \left\{ f(x) = v_0 + \sum_i v_i x_i + \sum_{i \leq j} v_{i,j} x_i x_j \mid v \in \mathbb{R}^{d_S} \right\}, \quad (4.8)$$

and, in the large data regime ($N > d_S$), identifying quadratic dependencies between variables becomes equivalent to (1) adding nodes to the hypergraph corresponding to secondary variables obtained from primary variables x_i through known functions (for (4.7), these secondary variables are the quadratic monomials $x_i x_j$, see Fig. 17.(a)), and (2) identifying affine dependencies between the variables of the augmented hypergraph. The problem can, therefore, be reduced to the affine case discussed in Sec. 4.1. Indeed, as in the affine case, the manifold can then be approximated in the regime where the number of data points is larger than the dimension d_S of the feature map by (4.5), where

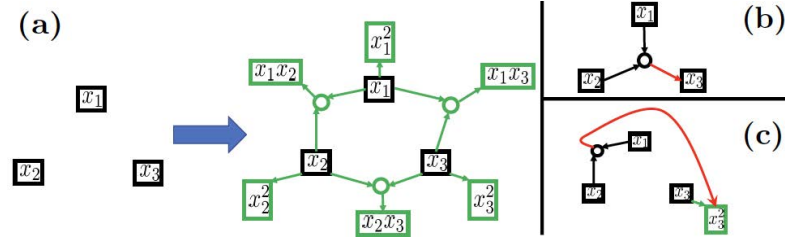


FIGURE 17. Feature map generalization

v_r, \dots, v_N are the eigenvectors of $C_N = (4.4)$ whose eigenvalues are zero (noiseless case) or smaller than some threshold $\epsilon > 0$ (noisy case).

Furthermore, the hypergraph representation of the manifold is equivalent to a feature map generalization of Row Echelon Form Reduction to nonlinear systems of equations. For instance, choosing x_3 as the dependent variable and x_1, x_2 as the free variables, $\mathcal{M} = \{x \in \mathbb{R}^3 \mid x_3 - 5x_1^2 + x_2^2 - x_1x_2 = 0\}$ can be represented as in Fig. 17.(b) where the round node represents the concatenated variable (x_1, x_2) and the red arrow represents a quadratic function. The generalization also enables the representation of implicit equations by selecting secondary variables as free variables. For instance, selecting x_3^2 as the free variable and x_1, x_2 as the free variables, $\mathcal{M} = \{x \in \mathbb{R}^3 \mid x_1^2 + x_2^2 + x_3^2 - 1 = 0\}$ can be represented as in Fig. 17.(c).

4.3. Kernel generalization and regularization. This feature-map extension of the affine case discussed in Sec. 4.2 can evidently be generalized to arbitrary degree polynomials and to other basis functions. However, as the dimension $d_{\mathcal{S}}$ of the range of the feature map ψ increases beyond the number N of data points, the problem becomes underdetermined: the data only provides partial information about the manifold, i.e., it is not sufficient to uniquely determine the manifold. Furthermore, if the dimension of the feature map is infinite, then we are always in that low data regime, and we have the additional difficulty that we cannot directly compute with that feature map. On the other hand, if $d_{\mathcal{S}}$ is finite (i.e., if the dictionary of basis functions is finite), then some elements of \mathcal{F} (some constraints defining the manifold \mathcal{M}) may not be representable or well approximated as equations of the form $v^T \psi(x) = 0$. To address these conflicting requirements, we need to kernelize and regularize the proposed approach (as done in interpolation).

4.3.1. The kernel associated with the feature map. To describe this kernelization, we assume that the feature map ψ maps \mathbb{R}^d to some Hilbert space \mathcal{S} that could be infinite-dimensional, and we write K for the kernel defined by that feature map. To be precise, we now consider the setting where the feature map ψ is a function from \mathbb{R}^d to a (possibly infinite-dimensional separable) Hilbert (feature) space \mathcal{S} endowed with the inner product $\langle \cdot, \cdot \rangle_{\mathcal{S}}$. To simplify notations, we will still write $v^T w$ for $\langle v, w \rangle_{\mathcal{S}}$ and vw^T for the linear operator mapping v' to $v \langle w, v' \rangle_{\mathcal{S}}$. Let

$$\mathcal{H} := \{v^T \psi(x) \mid v \in \mathcal{S}\} \quad (4.9)$$

be the space of functions mapping \mathbb{R}^d to \mathbb{R} defined by the feature map ψ . To avoid ambiguity, assume (without loss of generality) that the identity $v^T \psi(x) = w^T \psi(x)$ holds for all $x \in \mathbb{R}^d$ if and only if $v = w$. It follows that for $f \in \mathcal{H}$ there exists a unique $v \in \mathcal{S}$ such that $f = v^T \psi$. For $f, g \in \mathcal{H}$ with $f = v^T \psi$ and $g = w^T \psi$, we can then define

$$\langle f, g \rangle_{\mathcal{H}} := v^T w. \quad (4.10)$$

Observe that \mathcal{H} is a Hilbert space endowed with the inner product $\langle \cdot, \cdot \rangle_{\mathcal{H}}$. For $x, x' \in \mathcal{X}$, write

$$K(x, x') := \psi(x)^T \psi(x'), \quad (4.11)$$

for the kernel defined by ψ and observe that $(\mathcal{H}, \langle \cdot, \cdot \rangle_{\mathcal{H}})$ is the RKHS defined by the kernel K (which is assumed to contain \mathcal{F} in Problem 1). Observe in particular that for $f = v^T \psi \in \mathcal{H}$, K satisfies the reproducing property

$$\langle f, K(x, \cdot) \rangle_{\mathcal{H}} = v^T \psi(x) = f(x). \quad (4.12)$$

4.3.2. Complexity Reduction with Kernel PCA Variant. We will now show that the feature-map PCA variant of Sec. 4.1 (characterizing the subspace of $f \in \mathcal{H}$ such that $f(X) = 0$) can be kernelized as a variant of kernel PCA [23]. To describe this write $K(X, X)$ for the $N \times N$ matrix with entries $K(X_i, X_j)$. Write $\lambda_1 \geq \lambda_2 \geq \dots \geq \lambda_r > 0$ for the nonzero eigenvalues of $K(X, X)$ indexed in decreasing order and write $\alpha_{\cdot, i}$ for the corresponding unit-normalized eigenvectors, i.e.

$$K(X, X)\alpha_{\cdot, i} = \lambda_i \alpha_{\cdot, i} \text{ and } |\alpha_{\cdot, i}| = 1. \quad (4.13)$$

Write $f(X)$ for the N vector with entries $f(X_s)$. For $i \leq r$, write

$$\phi_i := \sum_{s=1}^N \delta_{X_s} \alpha_{s, i} \quad (4.14)$$

and

$$f(\phi_i) := \sum_{s=1}^N f(X_s) \alpha_{s, i}. \quad (4.15)$$

Write $f(\phi)$ for the r vector with entries $f(\phi_i)$.

Then, we have the following proposition.

Proposition 4.1. *The subspace of functions $f \in \mathcal{H}$ such that $f(\phi) = 0$ is equal to the subspace of $f \in \mathcal{H}$ such that $f(X) = 0$. Furthermore for $f \in \mathcal{H}$ with feature map representation $f = v^T \psi$ with $v \in \mathcal{S}$ we have the identity (where $C_N = (4.4)$)*

$$v^T C_N v = |f(\phi)|^2 = |f(X)|^2. \quad (4.16)$$

Proof. Write $\hat{\lambda}_1 \geq \hat{\lambda}_2 \geq \dots \geq \hat{\lambda}_r > 0$ for the nonzero eigenvalues of $C_N = (4.4)$ indexed in decreasing order. Write v_1, \dots, v_r for the corresponding eigenvectors, i.e.,

$$C_N v_i = \hat{\lambda}_i v_i. \quad (4.17)$$

Observing that

$$C_N = \sum_{i=1}^r \hat{\lambda}_i v_i v_i^T \quad (4.18)$$

we deduce that the zero-eigenspace of C_N is the set of vectors $v \in \mathcal{S}$ such that $v^T v_i = 0$ for $i = 1, \dots, r$. Write $f_i := v_i^T \psi$. Observe that for $f = v^T \psi$, we have $v_i^T v = \langle f_i, f \rangle_K$. Multiplying (4.17) by $\psi^T(x)$ implies

$$\sum_{s=1}^N K(x, X_s) f_i(X_s) = \hat{\lambda}_i f_i(x) \quad (4.19)$$

(4.19) implies that for $f = v^T \psi$

$$v_i^T v = \sum_{s=1}^N \hat{\lambda}_i^{-1} f_i(X_s) \langle K(\cdot, X_s), f \rangle_K = \sum_{s=1}^N \hat{\lambda}_i^{-1} f_i(X_s) f(X_s) \quad (4.20)$$

where we have used the reproducing property (4.12) of K in the last identity. Write

$$\hat{\alpha}_{s,i} := \lambda_i^{-1/2} f_i(X_s). \quad (4.21)$$

Using (4.19) with $x = X_{s'}$ implies that $\hat{\alpha}_{\cdot,i}$ is an eigenvector of the $N \times N$ matrix $K(X, X)$ with eigenvalue $\hat{\lambda}_i$. Taking $f = f_i$ in (4.20) implies that $1 = v_i^T v_i = |\hat{\alpha}_{\cdot,i}|^2$. Therefore, the $\hat{\alpha}_{\cdot,i}$ are unit-normalized. Summarizing, this analysis (closely related to the one found in kernel PCA [23]) shows that the nonzero eigenvalues of $K(X, X)$ coincide with those of C_N and we have $\hat{r} = r$, $\hat{\lambda}_i = \lambda_i$ and $\hat{\alpha}_{\cdot,i} = \alpha_{\cdot,i}$. Furthermore, (4.20) and (4.21) imply that for $i \leq r$, $v \in \mathcal{S}$ and $f = v^T \psi$, we have

$$v_i^T v = \lambda_i^{-1/2} f(X) \alpha_{\cdot,i}. \quad (4.22)$$

The identity (4.22) then implies (4.16). \square

Remark 4.2. *As in PCA the dimension/complexity of the problem can be further reduced by truncating ϕ to $\phi^l = (\phi_1, \dots, \phi_{r'})$ where $r' \leq r$ is identified as the smallest index i such that $\lambda_i/\lambda_1 < \epsilon$ where $\epsilon > 0$ is some small threshold.*

4.3.3. Kernel Mode Decomposition. When the feature map ψ is infinite-dimensional, the data only provides partial information about the constraints defining the manifold in the sense that $f(X) = 0$ or equivalently $f(\phi) = 0$ is a necessary but not sufficient condition for the zero level set of f to be a valid constraint for the manifold (for f to be such that $f(x) = 0$ for all $x \in \mathcal{M}$). So we are faced with the following problems: (1) How to regularize? (2) How do we identify free and dependent variables? (3) How do we identify valid constraints for the manifold? The proposed solution will be based on the Kernel Mode Decomposition (KMD) framework introduced in [30].

Reminder on KMD. We will now present a quick reminder on KMD in the setting of the following mode decomposition problem. So, in this problem, we have an unknown function f^\dagger mapping some input space \mathcal{X} to the real line \mathbb{R} . We assume that this function can be written as a sum of m other unknown functions f_i^\dagger which we will call modes, i.e.,

$$f^\dagger = \sum_{i=1}^m f_i^\dagger. \quad (4.23)$$

We assume each mode f_i^\dagger to be an unknown element of some RKHS \mathcal{H}_{K_i} defined by some kernel K_i . Then we consider the problem in which given the data $f^\dagger(X) = Y$ (with

$(X, Y) \in \mathcal{X}^N \times \mathbb{R}^N$) we seek to approximate the m modes composing the target function f^\dagger . Then, we have the following theorem.

Theorem 4.3. [30] *Using the relative error in the product norm $\|(f_1, \dots, f_m)\|^2 := \sum_{i=1}^m \|f_i\|_{K_i}^2$ as a loss, the minimax optimal recovery of $(f_1^\dagger, \dots, f_m^\dagger)$ is (f_1, \dots, f_m) with*

$$f_i(x) = K_i(x, X)K(X, X)^{-1}Y, \quad (4.24)$$

where K is the additive kernel

$$K = \sum_{i=1}^m K_i. \quad (4.25)$$

The GP interpretation of this optimal recovery result is as follows. Let $\xi_i \sim \mathcal{N}(0, K_i)$ be m independent centered GPs with kernels K_i . Write ξ for the additive GP $\xi := \sum_{i=1}^m \xi_i$. (4.24) can be recovered by replacing the modes f_i^\dagger by independent centered GPs $\xi_i \sim \mathcal{N}(0, K_i)$ with kernels K_i and approximating the mode i by conditioning ξ_i on the available data $\xi(X) = Y$ where $\xi := \sum_{i=1}^m \xi_i$ is the additive GP obtained by summing the independent GPs ξ_i , i.e.,

$$f_i(x) = \mathbb{E}[\xi_i(x) \mid \xi(X) = Y]. \quad (4.26)$$

Furthermore (f_1, \dots, f_m) can also be identified as the minimizer of

$$\begin{cases} \text{Minimize} & \sum_{i=1}^m \|f_i\|_{K_i}^2 \\ \text{over} & (f_1, \dots, f_m) \in \mathcal{H}_{K_1} \times \dots \times \mathcal{H}_{K_m} \\ \text{s. t.} & (\sum_{i=1}^m f_i)(X) = Y. \end{cases} \quad (4.27)$$

The variational formulation (4.27) can be interpreted as a generalization of Tikhonov regularization which can be recovered by selecting $m = 2$, K_1 to be a smoothing kernel (such as a Matérn kernel) and $K_2(x, y) = \sigma^2 \delta(x - y)$ to be a white noise kernel.

Now, this abstract KMD approach [30] is associated with a quantification of how much each mode contributes to the overall data or how much each individual GP ξ_i explains the data. More precisely, the activation of the mode i or GP ξ_i can be quantified as

$$p(i) = \frac{\|f_i\|_{K_i}^2}{\|f\|_K^2}, \quad (4.28)$$

where $f = \sum_{i=1}^m f_i$. These activations $p(i)$ satisfy $p(i) \in [0, 1]$ and $\sum_{i=1}^m p(i) = 1$ they can be thought of as a generalization of Sobol sensitivity indices [40, 41, 25] to the nonlinear setting in the sense that they are associated with the following variance representation/decomposition [30] (writing $\langle \cdot, \cdot \rangle_K$ for the RKHS inner product induced by K):

$$\text{Var} [\langle \xi, f \rangle_K] = \|f\|_K^2 = \sum_{i=1}^m \|f_i\|_{K_i}^2 = \sum_{i=1}^m \text{Var} [\langle \xi_i, f \rangle_K] \quad (4.29)$$

Application to CHD, general case. Now, let us return to our original manifold approximation problem 1 in the kernelized setting of Sec. 4.3.1. Given the data X we cannot regress an element $f \in \mathcal{F}$ directly since the minimizer of $\|f\|_K^2 + \gamma^{-1} \|f(X)\|_{\mathbb{R}^N}^2$ is the null function. To identify the functions $f \in \mathcal{F}$, we need to decompose them into modes that can be interpreted as a generalization of the notion of free and dependent

variables. To describe this, assume that the kernel K can be decomposed as the additive kernel

$$K = K_a + K_s + K_z. \quad (4.30)$$

Then $\mathcal{H}_K = \mathcal{H}_{K_a} + \mathcal{H}_{K_s} + \mathcal{H}_{K_z}$ implies that for all function $f \in \mathcal{H}_K$, f can be decomposed as $f = f_a + f_s + f_z$ with $(f_a, f_s, f_z) \in \mathcal{H}_a \times \mathcal{H}_s \times \mathcal{H}_z$.

Example 4.4. *As a running example, take K to be the following additive kernel*

$$K(x, x') = 1 + \beta_1 \sum_i x_i x'_i + \beta_2 \sum_{i \leq j} x_i x_j x'_i x'_j + \beta_3 \prod_i (1 + k(x_i, x'_i)), \quad (4.31)$$

that is the sum of a linear kernel, a quadratic kernel and a fully nonlinear kernel. Take K_a to be the part of the linear kernel that depends only on x_1 , i.e.,

$$K_a(x, x') = \beta_1 x_1 x'_1. \quad (4.32)$$

Take K_s to be the part of the kernel that does not depend on x_1 , i.e.,

$$K_s = 1 + \beta_1 \sum_{i \neq 1} x_i x'_i + \beta_2 \sum_{i \leq j, i, j \neq 1} x_i x_j x'_i x'_j + \beta_3 \prod_{i \neq 1} (1 + k(x_i, x'_i)). \quad (4.33)$$

And take K_z to be the remaining portion,

$$K_z = K - K_a - K_s. \quad (4.34)$$

Therefore the following questions are equivalent:

- Given a function g_a in the RKHS \mathcal{H}_{K_a} defined by the kernel K_a is there a function f_s in the the RKHS \mathcal{H}_{K_s} defined by the kernel K_s such that $g_a(x) \approx f_s(x)$ for $x \in \mathcal{M}$?
- Given a function $g_a \in \mathcal{H}_{K_a}$ is there a function f in the RKHS \mathcal{H}_K defined by the kernel K such that $f(x) \approx 0$ for $x \in \mathcal{M}$ and such that its f_a mode is $-g_a$ and its f_z mode is zero?

Then, the natural answer to the questions and to those of Sec. 4.3.3 is to identify the modes of the constraint $f = f_a + f_s + f_z \in \mathcal{H}$ (such that $f(x) \approx 0$ for $x \in \mathcal{M}$) such that $f_a = -g_a$ and $f_z = 0$ by selecting f_s to be the minimizer of the following variational problem

$$\min_{f_s \in \mathcal{H}_s} \|f_s\|_{K_s}^2 + \frac{1}{\gamma} |(-g_a + f_s)(\phi)|^2. \quad (4.35)$$

This is equivalent to introducing the additive GP $\xi = \xi_a + \xi_s + \xi_z + \xi_n$ whose modes are the independent GPs $\xi_a \sim \mathcal{N}(0, K_a)$, $\xi_s \sim \mathcal{N}(0, K_s)$, $\xi_z \sim \mathcal{N}(0, K_z)$, $\xi_n \sim \mathcal{N}(0, \gamma\delta(x - y))$ (we use the label “n” in reference to “noise”), and then recovering f_s as

$$f_s = \mathbb{E}[\xi_s \mid \xi(X) = 0, \xi_a = -g_a, \xi_z = 0]. \quad (4.36)$$

Application to CHD, particular case. Taking $g_a(x) = x_1$ for our running example 4.4, the questions of Sec. 4.3.3 are, as illustrated in Sec. 2, equivalent to asking whether there exists a function $f_s \in \mathcal{H}_{K_s}$ that does not depend on x_1 (since K_s does not depend on x_1) such that

$$x_1 \approx f_s(x_2, \dots, x_d) \text{ for } x \in \mathcal{M}. \quad (4.37)$$

Therefore, the mode f_a can be thought of as a dependent mode (we use the label “a” in reference to “ancestors”), the mode f_s as a free mode (we use the label “s” in reference to “signal”), the mode f_z as a zero mode.

While our numerical illustrations have primarily focused on the scenario where g_a takes the form of $g_a(x) = x_i$, and we aim to express x_i as a function of other variables, the generality of our framework is motivated by its potential to recover implicit equations. For example, consider the implicit equation $x_1^2 + x_2^2 = 1$, which can be retrieved by setting the mode of interest to be $g_a(x) = x_1^2$ and allowing f_s to depend only on the variable x_2 .

4.3.4. Signal-to-noise ratio. Now, we are led to the following question: since the mode f_s (the minimizer of (4.35)) always exists and is always unique, how do we know that it leads to a valid constraint? To answer that question, we compute the activation of the GPs used to regress the data. We write

$$\mathcal{V}(s) := \|f_s\|_{K_s}^2, \quad (4.38)$$

for the activation of the signal GP ξ_s and

$$\mathcal{V}(n) := \frac{1}{\gamma} |(-g_a + f_s)(X)|^2 \quad (4.39)$$

for the activation of the noise GP ξ_n , and then these allow us to define a signal-to-noise ratio defined as

$$\frac{\mathcal{V}(s)}{\mathcal{V}(s) + \mathcal{V}(n)}. \quad (4.40)$$

Note that this corresponds to activation ratio of the noise GP defined in (4.28). This ratio can then be used to test the validity of the constraint in the sense that if $\mathcal{V}(s)/(\mathcal{V}(s) + \mathcal{V}(n)) > \tau$ (with $\tau = 0.5$ as a prototypical example), then the data is mostly explained by the signal GP and the constraint is valid. If $\mathcal{V}(s)/(\mathcal{V}(s) + \mathcal{V}(n)) < \tau$, then the data is mostly explained by the noise GP and the constraint is not valid.

4.3.5. Iterating by removing the least active modes from the signal. If the constraint is valid, then we can next compute the activation of the modes composing the signal. To describe this, we assume that the kernel K_s can be decomposed as the additive kernel

$$K_s = K_{s,1} + \cdots + K_{s,m}, \quad (4.41)$$

which results in $\mathcal{H}_{K_s} = \mathcal{H}_{K_{s,1}} + \cdots + \mathcal{H}_{K_{s,m}}$, which results in the fact that $\forall f_s \in \mathcal{H}_s$, f_s can be decomposed as

$$f_s = f_{s,1} + \cdots + f_{s,m}, \quad (4.42)$$

with $f_{s,i} \in \mathcal{H}_{K_{s,i}}$. The activation of the mode i can then be quantified as $p(i) = \|f_{s,i}\|_{K_{s,i}}^2 / \|f_s\|_{K_s}^2$, which combined with $\|f_s\|_{K_s}^2 = \sum_{i=1}^m \|f_{s,i}\|_{K_{s,i}}^2$ leads to $\sum_{i=1}^m p(i) = 1$.

As our running example 4.4, we can decompose $K_s = (4.33)$ as the sum of an affine kernel, a quadratic kernel, and a fully nonlinear kernel, i.e., $m = 3$, $K_{s,1} = 1 + \beta_1 \sum_{i \neq 1} x_i x'_i$, $K_{s,2} = \beta_2 \sum_{i \leq j, i, j \neq 1} x_i x_j x'_i x'_j$ and $K_{s,3} = \beta_3 \prod_{i \neq 1} (1 + k(x_i, x'_i))$.

As another example for our running example, we can take K_s to be the sum of the portion of the kernel that does not depend on x_1 and x_2 and the remaining portion, i.e., $m = 2$, $K_{s,1} = 1 + \beta_1 \sum_{i \neq 1, 2} x_i x'_i + \beta_2 \sum_{i \leq j, i, j \neq 1, 2} x_i x_j x'_i x'_j + \beta_3 \prod_{i \neq 1, 2} (1 + k(x_i, x'_i))$ and $K_{s,2} = K_s - K_{s,1}$.

Then, we can order these sub-modes from most active to least active and create a new kernel K_s by removing the least active modes from the signal and adding them to the

mode that is set to be zero. To describe this, let $\pi(1), \dots, \pi(m)$ be an ordering of the modes by their activation, i.e., $\|f_{s,\pi(1)}\|_{K_{s,\pi(1)}}^2 \geq \|f_{s,\pi(2)}\|_{K_{s,\pi(2)}}^2 \geq \dots$.

Writing $K_t = \sum_{i=r+1}^m K_{s,\pi(i)}$ for the additive kernel obtained from the least active modes (with $r+1 = m$ as the value used for our numerical implementations), we update the kernels K_s and K_z by assigning the least active modes from K_s to K_z , i.e., $K_s - K_t \rightarrow K_s$ and $K_z + K_t \rightarrow K_z$ (we zero the least active modes).

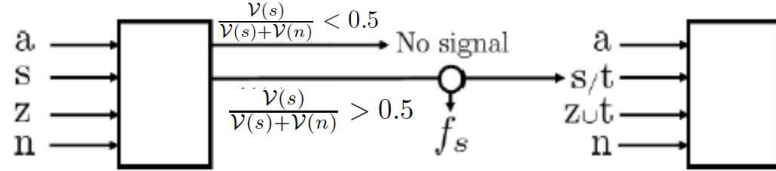


FIGURE 18. Iterating by removing the least active modes from the signal

Finally, we can iterate the process. This iteration can be thought of as identifying the structure of the hypergraph by placing too many hyperedges and removing them according to the activation of the underlying GPs.

For our running example 4.4, where we try to identify the ancestors of the variable x_1 , if the sub-mode associated with the variable x_2 is found to be least active, then we can try to remove x_2 from the list of ancestors and try to identify x_1 as a function of x_3 to x_d . This is equivalent to selecting $K_a(x, x') = \beta_1 x_1 x'_1$,

$$K_{s/t} = 1 + \beta_1 \sum_{i \neq 1,2} x_i x'_i + \beta_2 \sum_{i \leq j, i, j \neq 1,2} x_i x_j x'_i x'_j + \beta_3 \prod_{i \neq 1,2} (1 + k(x_i, x'_i)), \quad (4.43)$$

and $K_{z \cup t} = K - K_a - K_{s/t}$ to assess whether there exists a function $f_s \in \mathcal{H}_K$ that does not depend on x_1 and x_2 s.t. $x_1 \approx f_s(x_3, \dots, x_d)$ for $x \in \mathcal{M}$.

4.3.6. Alternative determination of the list of ancestors. The Sec. 4.3.4 and 4.3.5 approach to determining the list of ancestors of a given node is to use a fixed threshold (e.g., $\tau = 0.5$) to prune nodes. In this approach, we propose an alternative approach that mimics the strategy employed in Principal Component Analysis (PCA) for deciding which modes should be kept and which ones should be removed. The PCA approach is to order the modes in decreasing order of eigenvalues/variance and (1) either keep the smallest number modes holding/explaining a given fraction (e.g., 90%) of the variance in the data, (2) or use an inflection point/sharp drop in the decay of the eigenvalues to select which modes should be kept. Here, we propose a similar strategy. First we employ an alternative determination of the least active mode: we iteratively remove the mode that leads to the smallest increase in noise-to-signal ratio, i.e., we remove the mode t such that,

$$t = \operatorname{argmin}_t \frac{\mathcal{V}(n)}{\mathcal{V}(s/t) + \mathcal{V}(n)}. \quad (4.44)$$

For our running example 4.4 in which we try to find the ancestors of the variable x_1 this is equivalent to removing the variables or node t whose removal leads to the smallest loss

in signal-to-noise ratio (or increase in noise-to-signal ratio) by selecting

$$K_{s/t} = 1 + \beta_1 \sum_{i \neq 1, t} x_i x'_i + \beta_2 \sum_{i \leq j, i, j \neq 1, t} x_i x_j x'_i x'_j + \beta_3 \prod_{i \neq 1, t} (1 + k(x_i, x'_i)).$$

Next, we iterate this process, and we plot (a) the noise-to-signal ratio, and (b) the increase in noise-to-signal ratio as a function of the number of ancestors ordered according to this iteration. Fig. 12 illustrates this process and shows that the removal of an essential node leads to a sharp spike in increase in the noise-to-signal ratio (the noise-to-signal ratio jumps from approximately 50-60% to 99%). The identification of this inflection point can be used as a method for effectively and reliably pruning ancestors (see Sec. 2.6 for a detailed illustration).

Algorithm 1 CHD by thresholding the signal-to-noise ratio

Input: Data D , set of nodes V , threshold τ ($\tau = 0.5$ as a default value)

Output: Learned hypergraph

```

1:  $D \leftarrow \text{NormalizeData}(D)$  // Normalize the data
2: for node  $\in V$  do
3:   for kernel  $\in$  ["linear", "quadratic", "nonlinear"] do // Find the kernel
4:     SetOfAncestors  $\leftarrow$  All other nodes
5:     SignalToNoiseRatio  $\leftarrow$  ComputeSignalToNoiseRatio(kernel, node,  $D$ )
6:     if SignalToNoiseRatio  $>$   $\tau$  then choose that kernel and exit the for loop
7:     else remove all ancestors from node
8:     end if
9:   end for
10:  while SignalToNoiseRatio  $>$   $\tau$  do // Prune ancestors
11:    Find least important ancestor
12:    Recompute SignalToNoiseRatio without ancestor
13:    if SignalToNoiseRatio  $>$   $\tau$  then Remove that ancestor
14:    end if
15:  end while
16: end for

```

5. Algorithm pseudocode.

Our overall method is summarized in the pseudocode Alg. 1 and Alg. 2 that we will now describe. Alg. 1 takes the data D (encoded into the matrix X in Sec. 4.3 and 6) and the set of nodes V as an input and produces, as described in Sec. 4.3, for each node $i \in V$ its set of minimal ancestors A_i and the simplest possible function f_i such that $x_i \approx f_i((x_j)_{j \in A_i})$. It employs the default threshold of 0.5 on the signal-to-noise ratios for its operations. Line 1 normalizes the data (via an affine transformation) so that the samples X_i are of mean zero and variance 1. Given a node with index $i = 1$ in Line 2 (i runs through the set of nodes, and we select $i = 1$ for ease of presentation), the command in Line 3 refers to selecting a signal kernel of the form $K_s = (4.33)$ (where k is selected to be a vanilla RBF kernel such as Gaussian or Matérn), with $1 \geq \beta_1 > 0 = \beta_2 = \beta_3$ for the

linear kernel, $1 \geq \beta_1 \geq \beta_2 > 0 = \beta_3$ for the quadratic kernel and $1 \geq \beta_1 \geq \beta_2 \geq \beta_3 > 0$ for the fully nonlinear (interpolative) kernel. The `ComputeSignalToNoiseRatio` function in Line 5 computes the signal-to-noise ratio with $g_a(x) = x_1$ and with the kernel selected in Line 3. The value of γ is selected automatically by maximizing the variance of the histogram of eigenvalues of D_γ as described in Sec. 6.2 (with the kernel $K = K_s = (4.33)$ selected in Line 3 and $Y = g_a(X)$ with $g_a(x) = x_1$). The value of γ is re-computed whenever a node is removed from the list of ancestors, and K_s is nonlinear. Lines 11, 12 and 13 are described in Sec. 4.3.5. They correspond to iteratively identifying the ancestor node t contributing the least to the signal and removing that node from the set of ancestors of the node 1 if the removal of that node t does not send the signal-to-noise ratio below the default threshold 0.5.

Algorithm 2 CHD by inflection point in the noise-to-signal ratio

Input: Data D , set of nodes V , threshold τ ($\tau = 0.5$ as a default value)

Output: Learned hypergraph

```

1:  $D \leftarrow \text{NormalizeData}(D)$  // Normalize the data
2: for node  $\in V$  do
3:   for kernel  $\in$  ["linear", "quadratic", "nonlinear"] do // Find the kernel
4:     SetOfAncestors  $\leftarrow$  All other nodes
5:     SignalToNoiseRatio  $\leftarrow$  ComputeSignalToNoiseRatio(kernel, node,  $D$ )
6:     if SignalToNoiseRatio  $> \tau$  then choose that kernel and exit the for loop
7:     else remove all ancestors from node
8:     end if
9:   end for
10:  q  $\leftarrow$  Cardinal(All other nodes)
11:  SetOfAncestors(q)  $\leftarrow$  All other nodes
12:  while q  $\geq 1$  do
13:    NoiseToSignalRatio(q)  $\leftarrow$  ComputeNoiseToSignalRatio(kernel, node,  $D$ )
14:    LeastImportantAncestor  $\leftarrow$  Find least important ancestor in
    SetOfAncestors(q)
15:    SetOfAncestors(q - 1)  $\leftarrow$  SetOfAncestors(q)  $\setminus$  LeastImportantAncestor
16:    q  $\leftarrow$  q - 1
17:  end while
18:   $q^\dagger \leftarrow$  Inflection point in ( $q \rightarrow \text{NoiseToSignalRatio}(q)$ ) or spike in ( $q \rightarrow$ 
    NoiseToSignalRatio( $q$ ) - NoiseToSignalRatio( $q - 1$ ))
19:  FinalSetOfAncestors  $\leftarrow$  SetOfAncestors( $q^\dagger$ )
20: end for

```

Algorithm 2 distinguishes itself from Algorithm 1 in its approach to pruning ancestors based on signal-to-noise ratios. Instead of using a default threshold of 0.5 like Algorithm 1, Algorithm 2 computes the noise-to-signal ratio, represented as $\frac{\mathcal{V}(n)}{\mathcal{V}(s)+\mathcal{V}(n)}(q)$. This ratio is calculated as a function of the number q of ancestors, which are ordered based on their decreasing contribution to the signal. The detailed methodology behind this computation can be found in Section 4.3.6 and is visually depicted in Figure 13. The final number q of

ancestors is then determined by finding the value that maximizes the difference between successive noise-to-signal ratios, $\frac{\mathcal{V}(n)}{\mathcal{V}(s)+\mathcal{V}(n)}(q+1) - \frac{\mathcal{V}(n)}{\mathcal{V}(s)+\mathcal{V}(n)}(q)$.

6. Analysis of the signal-to-noise ratio test.

6.1. The signal-to-noise ratio depends on the prior on the level of noise. The signal-to-noise ratio (4.40) depends on the value of γ , which is the variance prior on the level of noise. The goal of this subsection is to answer the following two questions: (1) How do we select γ ? (2) How do we obtain a confidence level for the presence of a signal? Or equivalently for a hyperedge of the hypergraph? To answer these questions, we will now analyze the signal-to-noise ratio in the following regression problem in which we seek to approximate the unknown function $f^\dagger : \mathcal{X} \rightarrow \mathbb{R}$ based on noisy observations

$$f^\dagger(X) + \sigma Z = Y \quad (6.1)$$

of its values at collocation points X_i ($(X, Y) \in \mathcal{X}^N \times \mathbb{R}^N$, $Z \in \mathbb{R}^N$, and the entries Z_i of Z are i.i.d $\mathcal{N}(0, 1)$). Assuming σ^2 to be unknown and writing γ for a candidate for its value, recall that the GP solution to this problem is approximate f^\dagger by interpolating the data with the sum of two independent GPs, i.e.,

$$f(x) = \mathbb{E}[\xi(x)|\xi(X) + \sqrt{\gamma}Z = Y], \quad (6.2)$$

where $\xi \sim \mathcal{N}(0, K)$ is the GP prior for the signal f^\dagger and $\sqrt{\gamma}Z \sim \mathcal{N}(0, \gamma I_N)$ is the GP prior for the noise σZ in the measurements. Following Sec. 4.3.3 f can also be identified as a minimizer of

$$\text{minimize}_{f'} \|f'\|_K^2 + \frac{1}{\gamma} \|f'(X) - Y\|_{\mathbb{R}^N}^2, \quad (6.3)$$

the activation of the signal GP can be quantified as $s = \|f\|_K^2$, the activation of the noise GP can be quantified as $\mathcal{V}(n) = \frac{1}{\gamma} \|f(X) - Y\|_{\mathbb{R}^N}^2$. We can then define the noise to signal ratio $\frac{\mathcal{V}(n)}{\mathcal{V}(s)+\mathcal{V}(n)}$, which admits the following representer formula,

$$\frac{\mathcal{V}(n)}{\mathcal{V}(s) + \mathcal{V}(n)} = \gamma \frac{Y^T (K(X, X) + \gamma I)^{-2} Y}{Y^T (K(X, X) + \gamma I)^{-1} Y}. \quad (6.4)$$

Observe that when applied to the setting of Sec. 4.3.4, this signal-to-noise ratio is calculated with $K = K_s$ and $Y = g_a(X)$.

Now we have the following proposition, which follows from (6.4).

Proposition 6.1. *It holds true that $\frac{\mathcal{V}(n)}{\mathcal{V}(s)+\mathcal{V}(n)} \in [0, 1]$, and if $K(X, X)$ has full rank,*

$$\lim_{\gamma \downarrow 0} \frac{\mathcal{V}(n)}{\mathcal{V}(s) + \mathcal{V}(n)} = 0 \text{ and } \lim_{\gamma \uparrow \infty} \frac{\mathcal{V}(n)}{\mathcal{V}(s) + \mathcal{V}(n)} = 1. \quad (6.5)$$

Therefore, we are led to the following question: if the signal f^\dagger and the level of noise σ^2 are both unknown, how do we select γ to decide whether the data is mostly signal or noise?

6.2. How do we select the prior on the level of noise? Our answer to this question depends on whether the feature-map associated with the base kernel K is finite-dimensional or not.

6.2.1. When the kernel is linear, quadratic or associated with a finite-dimensional feature map.

If the feature-map associated with the base kernel K is finite-dimensional, then γ can be estimated from the data itself when the number of data-points is sufficiently large (at least larger than the dimension of the feature-space \mathcal{S}). A prototypical example (when trying to identify the ancestors of the variable x_1) is $K = K_s = (4.33)$ with $\beta_3 = 0$. In the general setting assume that $K(x, x') := \psi(x)^T \psi(x')$ where the range \mathcal{S} of ψ is finite-dimensional. Assume that f^\dagger belongs to the RKHS defined by ψ , i.e., assume that it is of the form $f^\dagger = v^T \psi$ for some v in the feature-space. Then (6.1) reduces to

$$v^T \psi(X) + \sigma Z = Y, \quad (6.6)$$

and, in the large data regime, σ^2 can be estimated by

$$\bar{\sigma}^2 := \frac{1}{N} \inf_{w \in \mathcal{S}} \|w^T \psi(X) - Y\|_{\mathbb{R}^N}^2. \quad (6.7)$$

Our strategy, when the feature map is finite-dimensional, is then to select

$$\gamma = N \bar{\sigma}^2 = \inf_{w \in \mathcal{S}} \|w^T \psi(X) - Y\|_{\mathbb{R}^N}^2. \quad (6.8)$$

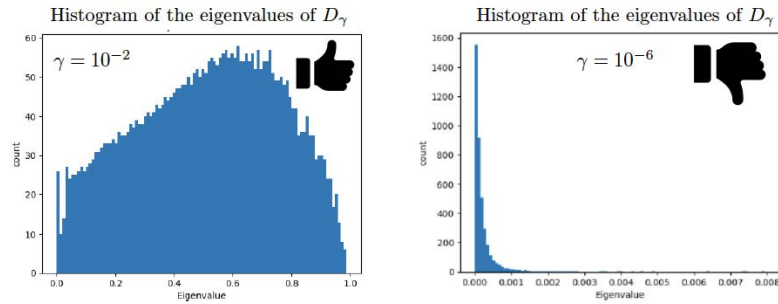


FIGURE 19. Histogram of the eigenvalues of $D_\gamma = (6.10)$ for $\gamma = 10^{-2}$ (good choice) and $\gamma = 10^{-6}$ (bad choice).

6.2.2. When the kernel is interpolatory (associated with an infinite-dimensional feature map).

If the feature-map associated with the base kernel K is infinite-dimensional (or has more dimensions than we have data points) then it can interpolate the data exactly and the previous strategy cannot be employed since the minimum of (6.7) is zero. A prototypical example (when trying to identify the ancestors of the variable x_1) is $K = K_s = (4.33)$ with $\beta_3 > 0$. In this situation, we do not attempt to estimate the level of noise σ but select a prior γ such that the resulting noise-to-signal ratio can effectively differentiate noise from signal. To describe this, observe that the noise-to-signal ratio (6.4) admits the representer formula

$$\frac{\mathcal{V}(n)}{\mathcal{V}(s) + \mathcal{V}(n)} = \frac{Y^T D_\gamma^2 Y}{Y^T D_\gamma Y}, \quad (6.9)$$

involving the $N \times N$ matrix

$$D_\gamma := \gamma(K(X, X) + \gamma I)^{-1}. \quad (6.10)$$

Observe that $0 \leq D_\gamma \leq I$, and

$$\lim_{\gamma \downarrow 0} D_\gamma = 0 \text{ and } \lim_{\gamma \uparrow \infty} D_\gamma = I. \quad (6.11)$$

Write (λ_i, e_i) for the eigenpairs of $K(X, X)$ ($K(X, X)e_i = \lambda_i e_i$) where the λ_i are ordered in decreasing order. Then the eigenpairs of D_γ are (ω_i, e_i) where

$$\omega_i := \frac{\gamma}{\gamma + \lambda_i}. \quad (6.12)$$

Note that the ω_i are contained in $[0, 1]$ and also ordered in decreasing order.

Writing \bar{Y}_i for the orthogonal projection of Y onto e_i , we have

$$\frac{\mathcal{V}(n)}{\mathcal{V}(s) + \mathcal{V}(n)} = \frac{\sum_{i=1}^n \omega_i^2 \bar{Y}_i^2}{\sum_{i=1}^n \omega_i \bar{Y}_i^2}, \quad (6.13)$$

It follows that if the histogram of the eigenvalues of D_γ is concentrated near 0 or near 1, then the noise-to-signal ratio is non-informative since the prior γ dominates it. To avoid this phenomenon, we select γ so that the eigenvalues of D_γ are well spread out in the sense that the histogram of its eigenvalues has maximum or near-maximum variance (see Fig. 19 for a good choice and a bad choice for γ). If the eigenvalues have an algebraic decay, then this is equivalent to taking γ to be the geometric mean of those eigenvalues. In practice, we use an off-the-shelf optimizer to obtain γ by maximizing the sample variance of $(\omega_i)_{i=1}^n$. If this optimization fails, we default to the median of the eigenvalues. This ensures a balanced, well-spread spectrum for D_γ , with half of the eigenvalues λ_i being lower and half being higher than the median.

6.2.3. Rationale for the choices of γ . The purpose of this section is to present a rationale for the proposed choices for γ in Sec. 6.2.1 and 6.2.2. For the choice Sec. 6.2.1, we present an asymptotic analysis of the signal-to-noise ratio in the setting of a simple linear regression problem. According to (6.8), γ must scale linearly in N ; this scaling is necessary to achieve a ratio that represents the signal-to-noise per sample. Without it (if γ remains bounded as a function of N), this scaling of the signal-to-noise would converge towards 0 as $N \rightarrow \infty$. To see how we will now consider a simple example in which we seek to linearly regress the variable y as a function of the variable x , both taken to be scalar (in which case $\psi(x) = x$). Assume that the samples are of the form $Y_i = aX_i + \sigma Z_i$ for $i = 1, \dots, N$, where $a, \sigma \neq 0$, the Z_i are i.i.d. $\mathcal{N}(0, 1)$ random variables, and the X_i satisfy $\frac{1}{N} \sum_{i=1}^N X_i = 0$ and $\frac{1}{N} \sum_{i=1}^N X_i^2 = 1$. Then, the signal-to-noise ratio is $\frac{\mathcal{V}(s)}{\mathcal{V}(s) + \mathcal{V}(n)}$ with $\mathcal{V}(s) = |v|^2$ and $\mathcal{V}(n) = \frac{1}{\gamma} \sum_{i=1}^N |vX_i - Y_i|^2$ and v is a minimizer of

$$\min_{v \in \mathbb{R}} |v|^2 + \frac{1}{\gamma} \sum_{i=1}^N |vX_i - Y_i|^2. \quad (6.14)$$

In asymptotic $N \rightarrow \infty$ regime, we have $v \approx \frac{aN}{\gamma + N}$ and

$$\frac{\mathcal{V}(s)}{\mathcal{V}(s) + \mathcal{V}(n)} \approx \frac{\frac{\gamma}{N} a^2}{-a^2(\gamma/N + 1) + (a^2 + \sigma^2)(\gamma/N + 1)^2}. \quad (6.15)$$

If γ is bounded independently from N , then $\frac{\mathcal{V}(s)}{\mathcal{V}(s) + \mathcal{V}(n)}$ converges towards zero as $N \rightarrow \infty$, which is undesirable as it does not represent a signal-to-noise ratio per sample. If $\gamma = N$,

then $\frac{\mathcal{V}(s)}{\mathcal{V}(s)+\mathcal{V}(n)} \approx \frac{a^2}{4\sigma^2+2a^2}$, which does not converge to 1 as $a \rightarrow \infty$ and $\sigma \rightarrow 0$, which is also undesirable. If γ is taken as in (6.8), then $\gamma \approx N\sigma^2$ and

$$\frac{\mathcal{V}(s)}{\mathcal{V}(s)+\mathcal{V}(n)} \approx \frac{a^2}{(\sigma^2+1)(a^2+\sigma^2+1)}, \quad (6.16)$$

which converges towards 0 as $\sigma \rightarrow \infty$ and towards $1/(1+\sigma^2)$ as $a \rightarrow \infty$, which has, therefore, the desired properties.

Moving to Sec. 6.2.2, because the kernel can interpolate the data exactly we can no longer use (6.7) to estimate the level of noise σ . For a finite-dimensional feature map ψ , with data (X, Y) , we can decompose $Y = v^T \psi(X) + \sigma Z$ into a signal part Y_s and noise part Y_n , s.t. $Y = Y_s + Y_n$. While Y_s belongs to the linear span of eigenvectors of $K(X, X)$ associated with non-zero eigenvalues, Y_n also activates the eigenvectors associated with the null space of $K(X, X)$ and the projection of Y onto that null-space is what allows us to derive γ in Sec. 6.2.1. Since in the interpolatory case, all eigenvalues are strictly positive, we need to choose which eigenvalues are associated with noise differently, as is described in the previous section. With a fixed γ , we see that if $\lambda_i \gg \gamma$, then $\omega_i \approx 0$, which contributes in (6.13) to yield a low noise-to-signal ratio. Similarly, if $\lambda_i \ll \gamma$, this eigenvalue yields a high noise-to-signal ratio. Thus, we see that the choice of γ assigns a noise level to each eigenvalue. While in the finite-dimensional feature map setting, this assignment is binary, here we perform soft thresholding using $\lambda \mapsto \gamma/(\gamma + \lambda)$ to indicate the level of noise of each eigenvalue. This interpretation sheds light on the selection of γ in equation (6.8). Let ψ represent the feature map associated with K . Assuming the empirical mean of $\psi(X_i)$ is zero, the matrix $K(X, X)$ corresponds to an unnormalized kernel covariance matrix $\psi^T(X)\psi(X)$. Consequently, its eigenvalues correspond to N times the variances of the $\psi(X_i)$ across various eigenspaces. After conducting Ordinary Least Squares regression in the feature space, if the noise variance is estimated as $\bar{\sigma}^2$, then any eigenspace of the normalized covariance matrix whose eigenvalue is lower than $\bar{\sigma}^2$ cannot be recovered due to the noise. Given this, we set the soft thresholding cutoff to be $\gamma = N\bar{\sigma}^2$ for the unnormalized covariance matrix $K(X, X)$.

6.3. Z-score/quantile bounds on the noise-to-signal ratio. If the noise is only comprised of noise, then an interval of confidence can be obtained on the noise-to-signal ratio. To describe this consider the problem of testing the null hypothesis $\mathbf{H}_0 : f^\dagger \equiv 0$ (there is no signal) against the alternative hypothesis $\mathbf{H}_1 : f^\dagger \neq 0$ (there is a signal). Under the null hypothesis \mathbf{H}_0 , the distribution of the noise-to-signal ratio (6.9) is known and it follows that of the random variable

$$B := \frac{Z^T D_\gamma^2 Z}{Z^T D_\gamma Z}. \quad (6.17)$$

Therefore, the quantiles of B can be used as an interval of confidence on the noise-to-signal ratio if \mathbf{H}_0 is true. More precisely, selecting β such that $\mathbb{P}[B \leq \beta_\alpha] \approx \alpha$ with $\alpha = 0.05$ as a prototypical example, we expect the noise to signal ratio (6.9) to be, under \mathbf{H}_0 , to be larger than β_α with probability $\approx 1 - \alpha$. The estimation of β requires Monte-Carlo sampling.

An alternative approach (in the large data regime) to using the quantile β_α is to use the Z-score

$$\mathcal{Z} := \frac{Y^T D_\gamma^2 Y}{Y^T D_\gamma Y} - \mathbb{E}[B], \quad (6.18)$$

after estimating $\mathbb{E}[B]$ and $\text{Var}[B]$ via Monte-Carlo sampling. In particular if \mathbf{H}_0 is true then $|\mathcal{Z}| \geq z_\alpha$ should occur with probability $\approx \alpha$ with $z_{0.1} = 1.65$, $z_{0.05} = 1.96$ and $z_{0.01} = 2.58$.

Remark 6.2. *Although the quantile β_α or the Z-score \mathcal{Z} can be employed to produce an interval of confidence on the noise-to-signal ratio under \mathbf{H}_0 we cannot use them as thresholds for removing nodes from the list of ancestors as discussed in Sec. 4.3.4. Indeed, observing a noise-to-signal ratio (6.9) below the threshold β_α does not imply that all the signal has been captured by the kernel; it only implies that some signal has been captured by the kernel K . To illustrate this point, consider the setting where one tries to approximate the variable x_1 as a function of the variable x_2 . If x_1 is not a function of x_2 , but of x_2 and x_3 , as in $x_1 = \cos(x_2) + \sin(x_3)$, then applying the proposed approach with Y encoding the values of x_1 , X encoding the values of x_2 , and the kernel K depending on x_2 could lead to a noise-to-signal ratio below β_α due to the presence of a signal in x_2 . Therefore, although we are missing the variable x_3 in the kernel K , we would still observe a possibly low noise-to-signal ratio due to the presence of some signal in the data. Summarizing if the data only contains noise then $\frac{\mathcal{V}(n)}{\mathcal{V}(s)+\mathcal{V}(n)} \geq \beta_\alpha$ should occur with probability $1 - \alpha$. If the event $\frac{\mathcal{V}(n)}{\mathcal{V}(s)+\mathcal{V}(n)} < \beta_\alpha$ is observed in the setting of $K = K_{s/t}$ (4.43) where we try to identify the ancestors of x_1 , then we can only deduce that x_3, \dots, x_d contain some signal but perhaps not all of it (we can use this as a criterion for pruning x_2).*

7. Numerical experiments.

We will now illustrate the proposed approach through numerical experiments that can be reproduced in the [Github repository of the paper](#).

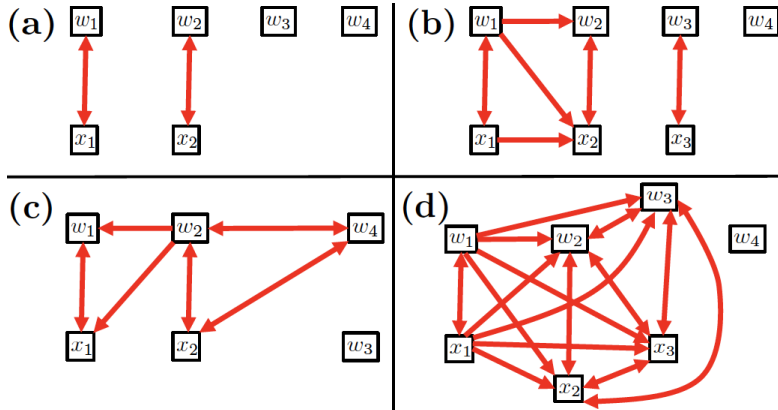


FIGURE 20. Algebraic equations examples.

7.1. Algebraic equations. The examples discussed in this section (Fig. 20.(a-d)) illustrate the application of the proposed approach to the recovery of functional dependencies from data satisfying hidden algebraic equations. In all these examples, we have $d = 6$ or $d = 7$ variables and $N = 1000$ samples from those variables. For $d = 6$ the variables are $w_1, w_2, w_3, w_4, x_1, x_2$. For $d = 7$ the variables are $w_1, w_2, w_3, w_4, x_1, x_2, x_3$. The samples from the variables w_1 to w_4 are i.i.d. $\mathcal{N}(0, 1)$ random variables, and the samples from x_1, x_2 (and x_3 for $d = 7$) are functionally dependent on the other variables. Although we have used Alg. 2 for the algebraic equations examples presented in this section, Alg. 1 yields the same results with the default signal-to-noise threshold $\tau = 0.5$.

7.1.1. Fig. 20.(a). In this example, $d = 6$ and the samples from x_1 and x_2 satisfy the equations

$$x_1 = w_1 \text{ and } x_2 = w_2. \quad (7.1)$$

Fig. 20.(a) shows the hypergraph recovered by the proposed approach using Alg. 2. The recovery is accurate and illustrates the one-to-one mappings between x_1 and w_1 , as well as between x_2 and w_2 .

7.1.2. Fig. 20.(b). In this example, $d = 7$ and the samples from x_1, x_2 and x_3 satisfy the equations

$$x_1 = w_1, \quad x_2 = x_1^2 + 1 + 0.1w_2, \text{ and } x_3 = w_3. \quad (7.2)$$

Fig. 20.(b) shows the hypergraph recovered by the proposed approach using Alg. 2. The results are notably accurate. The algorithm rightly pinpoints the direct correspondence between x_1 and w_1 , as well as between x_3 and w_3 . Yet, the efficiency of the algorithm is compromised when duplicate variables are present. For instance, given the quadratic kernel, even though x_2 can trace back its origin to either x_1 and w_2 or w_1 and w_2 , the algorithm recognizes x_1, w_1 , and w_2 as its ancestors. This underscores the significance of eliminating redundant variables when aiming to derive the sparsest and the most understandable graph.

7.1.3. Fig. 20.(c). In this example, $d = 6$ and the samples from x_1 and x_2 satisfy the equations

$$x_1 = w_1 w_2 \text{ and } x_2 = w_2 \sin(w_4). \quad (7.3)$$

Fig. 20.(c) shows the hypergraph recovered by the proposed approach using Alg. 2. The recovery is accurate. The underlying functional dependencies are inherently nonlinear and were not explicitly represented in our feature maps. By utilizing the fully nonlinear kernel (4.31), our approach identified the correct functional dependencies.

7.1.4. Fig. 20.(d). In this example, $d = 7$ and the samples from x_1, x_2 and x_3 satisfy the equations

$$x_1 = w_1, \quad x_2 = x_1^3 + 1 + 0.1w_2 \text{ and } x_3 = (x_1 + 2)^3 + 0.1w_3. \quad (7.4)$$

Fig. 20.(d) shows the hypergraph recovered with Alg. 2. Given our kernel selections (linear, quadratic, and fully nonlinear), one might anticipate an approximate recovery of the equations via the fully nonlinear kernel, especially considering the x_1^3 term. However, the method astutely identifies an alternative combination, permitting an exact recovery with the quadratic kernel. Notably, upon expanding $(x_1 + 2)^3$, it becomes evident that the cubic terms can be portrayed using linear and quadratic combinations of other nodes.

Such an automatic simplification in equations is undeniably profound. Such automatic discovery of simplifying equations is very powerful. Yet, it is worth mentioning that to achieve this exact quadratic recovery; we must consider more ancestors than originally denoted in (7.4). This emphasizes the notion that functional dependencies are profoundly influenced by the chosen function form, and our methodology discerns one of the potential dependencies.

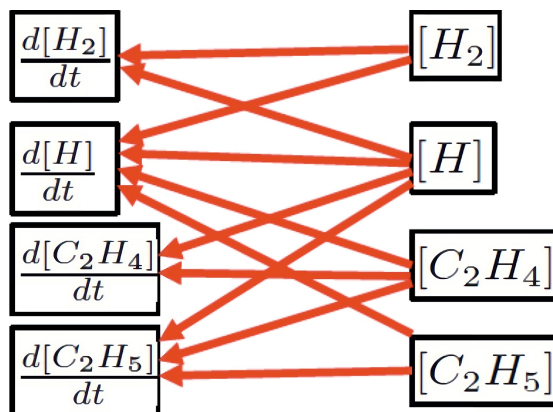


FIGURE 21. Output graph of the chemistry example. We observe perfect recovery of the equations in (7.5), which are also correctly identified as quadratic.

7.2. Chemical reaction network. We now consider the example described in Sec. 1.3.1 and taken from [19]. The proposed mechanism for the hydrogenation of ethylene (C_2H_4) to ethane (C_2H_6), is (writing $[H]$ for the concentration of H) modeled by the following system of differential equations

$$\begin{aligned}
 \frac{d[H_2]}{dt} &= -k_1[H_2] + k_{-1}[H]^2 \\
 \frac{d[H]}{dt} &= 2k_1[H_2] - 2k_{-1}[H]^2 - k_2[C_2H_4][H] - k_3[C_2H_5][H] \\
 \frac{d[C_2H_4]}{dt} &= -k_2[C_2H_4][H] \\
 \frac{d[C_2H_5]}{dt} &= k_2[C_2H_4][H] - k_3[C_2H_5][H]
 \end{aligned} \tag{7.5}$$

The primary variables are the concentrations $[H_2]$, $[H]$, $[C_2H_4]$ and $[C_2H_5]$ and their time derivatives $\frac{d[H_2]}{dt}$, $\frac{d[H]}{dt}$, $\frac{d[C_2H_4]}{dt}$ and $\frac{d[C_2H_5]}{dt}$. The computational hypergraph encodes the functional dependencies (7.5) associated with the chemical reactions. The hyperedges of the hypergraph are assumed to be unknown and the primary variables are assumed to be known. Given N samples from the graph of the form

$$([H_2](t_i), [H](t_i), [C_2H_4](t_i), [C_2H_5](t_i))_{i=1, \dots, N} \tag{7.6}$$

our objective is to recover the structure of the hypergraph given by (7.5), representing the functions by hyperedges. We create a dataset of the form (7.6) by integrating 50 trajectories of (7.5) for different initial conditions, and each equispaced 50 times from $t = 0$ to $t = 5$. The dataset is represented in Figure 5 (the time derivatives of concentrations are estimated by taking the derivatives of the interpolants of those concentrations). We impose the information that the derivative variables are function of the non-derivative variables to avoid ambiguity in the recovery, as (7.5) is not the unique representation of the functional relation between nodes in the graph. We implement Alg. 1 with weights $\beta = [0.1, 0.01, 0.001]$ for linear, quadratic, and nonlinear, respectively (Alg. 2 recovers the same hypergraph). The output graph can be seen in Fig. 21. We obtain a perfect recovery of the computational graph and a correct identification of the relations being quadratic.

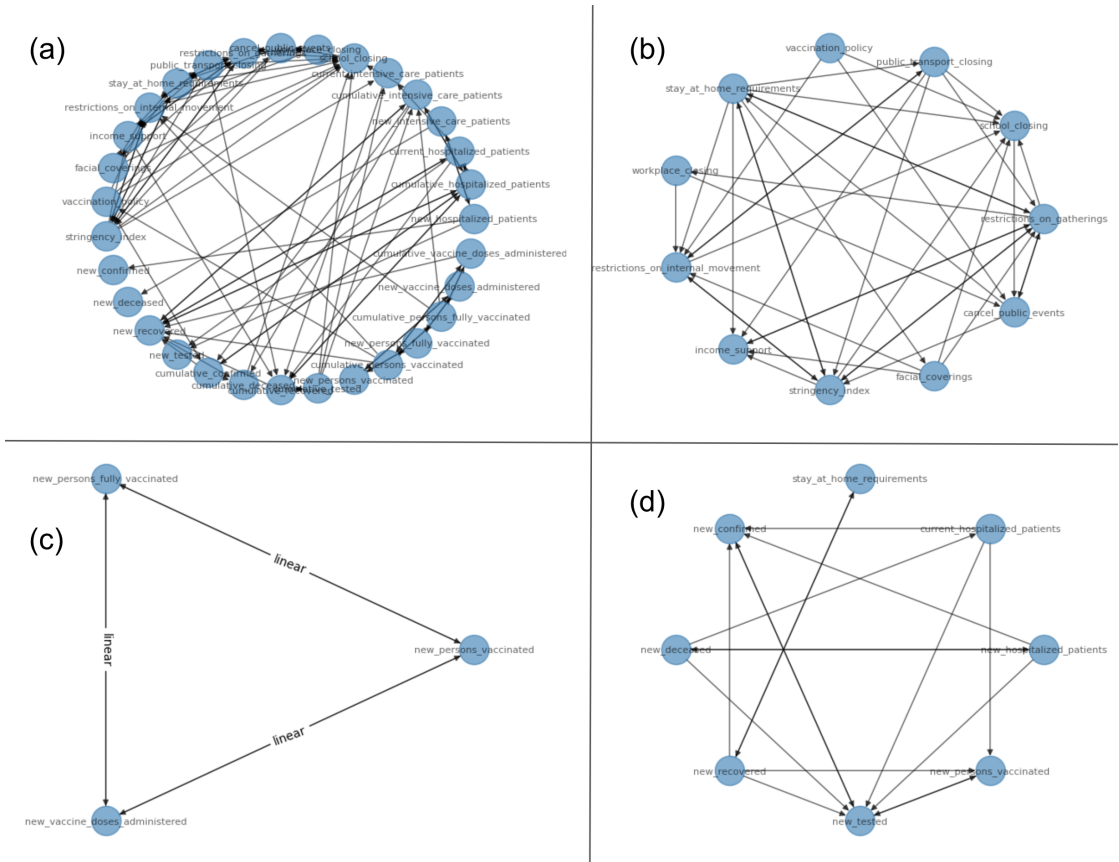


FIGURE 22. (a) Full retrieved graph. (b) Policy subgraph (c) “New intensive care patients” subgraph. (d) Recovered graph from the COVID-19 open data after removing redundant information.

7.3. The Google Covid 19 open data. This section uses the CHD framework as a statistical analysis tool to scrutinize COVID-19 open data, as detailed in Sec. 1.3.2.

Categorical data are treated as scalar values, with all variables scaled to achieve a mean of 0 and a variance of 1. We implement three distinct kernel types: linear, quadratic, and Gaussian, with a length scale of 1 for the latter. A weight ratio of 1/10 is assigned between kernels, signifying that the quadratic kernel is weighted ten times less than the linear kernel. Lastly, the noise parameter, γ , is determined using the optimal value outlined in Sec. 6.

Initially, a complete graph is constructed using all variables, depicted in Fig.22.(a). This construction is done using only linear and quadratic kernels. This is done to regularise our problem by choosing a feature map whose dimension is not too high. An example of the evolution of the signal-to-noise ratio we observe is given in Fig. 23. In this case, it is very clear where we need to stop pruning, as the jumping noise ratio is significant. A notably clustered section within the graph is observed upon examination. Fig.22.(b) offers an in-depth view of this cluster, revealing its representation of the government’s pandemic response. This evident clustering leads to the conclusion that the government either implemented multiple restrictive measures simultaneously or lifted them in unison. From the subgraph shown in Fig.22.(b), a few representative nodes for the cluster are selected, ones with few and serving as an ancestor to numerous nodes. The vaccination policy and stay-at-home requirements are deemed an apt choice in this context, especially given their impact on the population. Additionally, new vaccinations form a cluster (Fig. 22.(c)), displaying a linear relationship between nodes, signaling redundant information. Eliminating redundant nodes is vital for two reasons: firstly, it improves the graph’s readability, especially with 31 variables; secondly, it avoids hindering graph discovery. In an extreme case, treating two identical variables as distinct would result in one variable’s ancestor simply being its duplicate, yielding an uninformative graph.

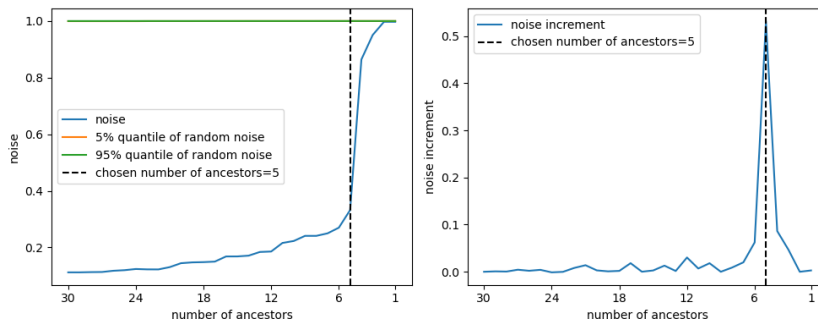


FIGURE 23. Evolution of the noise-to-signal ratio when pruning ancestors for the cumulative number of hospitalized patients.

Subsequently, the graph discovery algorithm is rerun, with reduced variables due to eliminating redundancy, ushering us into a predominantly noisy regime. With fewer variables available, we use additionally the Gaussian kernel. Two indicators are employed to navigate our discovery process: the signal-to-noise ratio and the Z-test. The former quantifies the degree to which our regression is influenced by noise, while the latter signals the existence of any signal. We follow the procedure in algorithm 2, resulting in the graph

presented in Fig. 22.(e). Here, some ancestor relationships are logical when interpreting using our experience of the COVID-19 pandemic. For instance, the number of new hospitalized and new deceased appear closely linked. Indeed, most recorded deaths are from people in a hospital. Additionally, it is observed that many ancestors are needed to explain the number of people tested. This number depends not only on the state of the epidemic but also on the government’s and the population’s reaction. Furthermore, many tests are conducted during holidays such as Christmas, regardless of the current pandemic status. This widespread testing complicates the ability to predict testing based solely on present variables. However, it is vital to acknowledge that not all relationships in the graph necessarily suggest causal connections. Our method determines graph edges based on functional relationships, not causal ones. Ultimately, this graph demonstrates sparsity, facilitating a superior understanding of the data’s underlying structure. Furthermore, the method allows us to identify and eliminate redundant information, enhancing clarity regarding the most pivotal trends observed.

7.4. Cell signaling network. Lastly, we apply the CHD framework to discover a hierarchy of functional dependencies in biological cellular signaling networks. We consider the problem discussed in Sec. 1.3.4 and illustrated in Fig. 7.(b). In this experiment, we use single-cell data consisting of the $d = 11$ phosphoproteins and phospholipids levels that were measured using flow cytometry. This dataset was studied from a probabilistic modeling perspective in previous works. While [34] learned a directed acyclic graph to encode causal dependencies, [13] learned an undirected graph of conditional independencies between the d molecule levels by assuming the underlying data follows a multivariate Gaussian distribution. The latter analysis encodes acyclic dependencies but does not identify directions. In this work, we aim to identify the functional dependencies without imposing strong distributional assumptions on the data.

To identify the ancestors of each node, we apply the algorithm in two stages. First, we learn the dependencies using only linear and quadratic kernels. Figure 24 left identifies the resulting graph learned given a subset of $N = 2,000$ samples chosen uniformly at random from the dataset. We observe that the graph identified by the algorithm consists of four disconnected clusters where the molecule levels in each cluster are closely related by linear or quadratic dependencies (all connections are linear except for the connection between Akt and PKA, which is quadratic). These edges match a subset of the edges found in the gold standard model identified in [34]. With perfect dependencies that have no noise, one can define constraints that reduce the total number of variables in the system. For this noisy dataset that, we treat these dependencies as forming groups of similar variables and introduce a hierarchical approach to learn the connections between groups.

Second, we run the graph discovery algorithm after grouping the molecules into clusters. For each node in the graph, we identified the ancestors of each node by constraining the dependence to be a subset of the clusters. In other words, when identifying the ancestors of a given node i in cluster C , the algorithm is only permitted to (1) use ancestors that do not belong to cluster C , and (2) include all or none of the variables in each cluster (j in cluster $D \neq C$ is listed as an ancestor if and only if all other nodes j' in

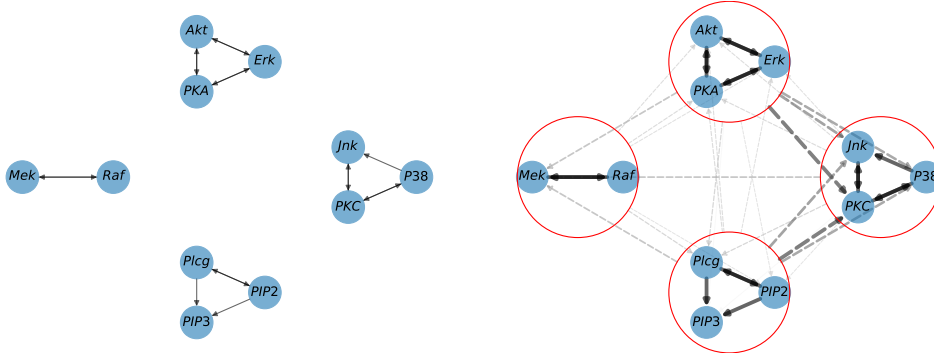


FIGURE 24. (Left) Graph identified based on linear and quadratic kernels. (Right) Graph identified with the proposed multi-level approach. Solid arrows represent the strong intra-cluster connections identified in the first level, and the dashed lines represent the relatively weaker connections between nodes and clusters identified in the second level. The width and grayscale intensities of each edge correspond to its signal-to-noise ratio.

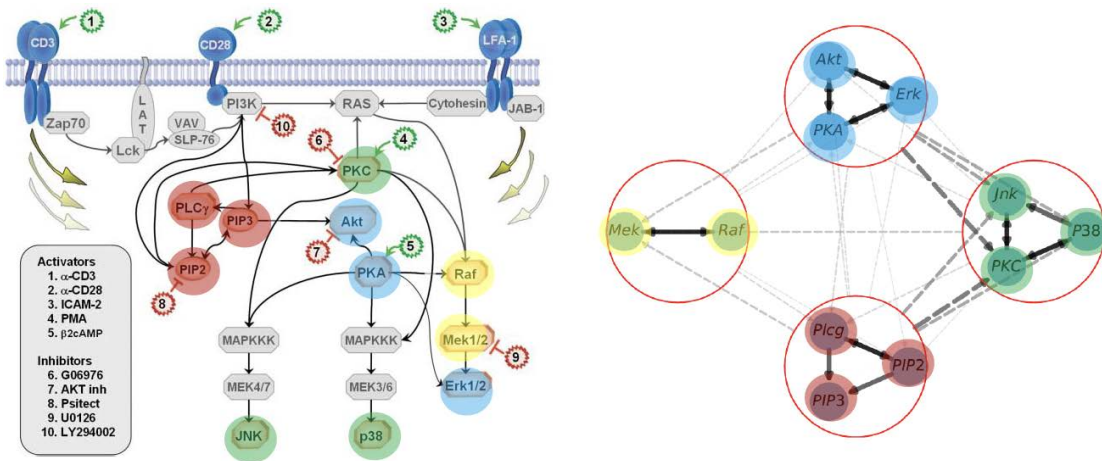


FIGURE 25. (Left) Graph identified in [34] where the nodes are colored based on their membership in a cluster. (Right) Graph identified with the proposed multi-level approach showing similar intra-cluster connections as the left figure as well as the dominant connections outside each cluster. We remind the reader that the arrows identified by the CHD framework encode functional dependence rather than causality.

cluster D are also listed as ancestors). The ancestors were identified using a Gaussian (fully nonlinear) kernel and the number of by ancestors were selected manually based on the inflection point in the noise-to-signal ratio. The resulting graph is depicted on the right side of Figure 24. Each edge is weighted based on its signal-to-noise ratio.

We observe that there is a stronger dependence of the Jnk, PKC, and P38 cluster on the PIP3, Plcg, and PIP2 cluster, which closely matches the gold standard model. As compared to approaches based on acyclic DAGs, however, the graph identified by our algorithm also contains feedback loops between the various molecule levels. Fig. 25 displays a side-by-side comparison between the graph generated in [34] and the graph identified with our method. To aid in this comparison, we have highlighted different clusters in distinct colors. We emphasize that while the Bayesian network analysis in [34] relied on the control of the sampling of the underlying variables (the simultaneous measurement of multiple phosphorylated protein and phospholipid components in thousands of individual primary human immune system cells, and perturbing these cells with molecular interventions), the reconstruction obtained by our method did not use this information and recovered functional dependencies rather than causal dependencies. Interestingly, the information recovered through our method appears to complement and enhance the findings presented in [34] (e.g., the linear and noiseless dependencies between variables in the JNK cluster is not something that could easily be inferred from the graph produced in [34]).

7.5. Discussions. In our numerical experiments, we observe that the proposed algorithm maintains robustness with respect to the selection of the signal kernel, i.e., the β_i in the kernel (2.7). Furthermore, the noise prior variance γ identified by our algorithm is very close to the regularization term that minimizes cross-validation mean square loss. More precisely, the identification of functional dependencies between variables relies on regressing input-output data (X, Y) for the signal function f with a kernel K and a nugget term γ ($f(\cdot) = K(\cdot, X)(K(X, X) + \gamma I)^{-1}Y$). Writing (X^c, Y^c) for a subset of the input-output data, $f^c(\cdot) = K(\cdot, X^c)(K(X^c, X^c) + \gamma I)^{-1}Y^c$ for the corresponding kernel ridge regressor, and γ_c for the minimizer of L^2 error $\|Y - f^c(X)\|$, the value of γ selected by our algorithm is very close to γ_c . This suggests that one could also use cross-validation (applied to recover the signal function between a given node and a group of nodes in computing a noise-to-signal ratio) to select γ .

We also observe that forming clusters from highly interdependent variables helps to obtain a sparser graph. Additionally, the precision of the pruning process is enhanced by avoiding the division of node activation within the cluster among its separate constituents. We employed this strategy in the recovery of the gene expression graph in Sec. 7.4. See Sec. 7.1.2 for an algebraic equation example where this strategy would have enhanced the recovery but was not used. We also note from the algebraic equation recovery examples of Sec. 7.1.4 that we can only hope to recover equivalent equations, and the type of equations recovered depends on the kernel employed for the signal.

8. Conclusion

We have developed a comprehensive Gaussian Process framework for solving Type 3 (hypergraph discovery) problems, which is interpretable and amenable to analysis. The breadth and complexity of Type 3 problems significantly surpass those encountered in Type 2 (hypergraph completion), and the initial numerical examples we present serve as a motivation for the scope of Type 3 problems and the broader applications made possible by this approach. Our proposed algorithm is designed to be fully autonomous, yet it offers

the flexibility for manual adjustments to refine the graph’s structure recovery, as detailed Sec. 7.4. Additionally, our method eliminates the need for a predetermined ordering of variables, a common requirement in acyclic probabilistic models where determining an optimal order is an NP-hard problem usually tackled using heuristic approaches. Furthermore, our approach can actually be utilized to generate such an ordering by quantifying the strength of the connections it recovers. The Uncertainty Quantification properties of the underlying Gaussian Processes are integral to the method and could also be employed to quantify uncertainties in the structure of the recovered graph. While the uncertainty quantification (UQ) properties of Gaussian Processes (GPs) lack a direct equivalent in Deep Learning, generalizing our approach to encompass richly hyperparameterized kernels could facilitate its extension to Deep Learning type connections between variables. This is achievable by interpreting neural networks as hyperparameterized feature maps.

Acknowledgements. HO, TB, PB, XY, and RB acknowledge support from the Air Force Office of Scientific Research under MURI award number FA9550-20-1-0358 (Machine Learning and Physics-Based Modeling and Simulation). Additionally, HO, TB, and PB acknowledge support by the Department of Energy under award number DE-SC0023163 (SEA-CROGS: Scalable, Efficient and Accelerated Causal Reasoning Operators, Graphs and Spikes for Earth and Embedded Systems) and by the Jet Propulsion Laboratory, California Institute of Technology, under a contract with the National Aeronautics and Space Administration. HO and PB further acknowledge support by Beyond Limits (Learning Optimal Models) through CAST (The Caltech Center for Autonomous Systems and Technologies). TB acknowledges support from the Kortschak Scholar Fellowship Program. NR acknowledges support from the JPL Researchers on Campus (JROC) program.

References

- [1] Ricardo Baptista, Youssef Marzouk, Rebecca E Morrison, and Olivier Zahm. Learning non-gaussian graphical models via hessian scores and triangular transport. *arXiv preprint arXiv:2101.03093*, 2021.
- [2] Pau Batlle, Yifan Chen, Bamdad Hosseini, Houman Owhadi, and Andrew M Stuart. Error analysis of kernel/gp methods for nonlinear and parametric pdes. *arXiv preprint arXiv:2305.04962*, 2023.
- [3] Pau Batlle, Matthieu Darcy, Bamdad Hosseini, and Houman Owhadi. Kernel methods are competitive for operator learning. *Journal of Computational Physics*, 2023.
- [4] Steven L Brunton, Joshua L Proctor, and J Nathan Kutz. Discovering governing equations from data by sparse identification of nonlinear dynamical systems. *Proceedings of the national academy of sciences*, 113(15):3932–3937, 2016.
- [5] Yifan Chen, Bamdad Hosseini, Houman Owhadi, and Andrew M Stuart. Solving and learning nonlinear pdes with gaussian processes. *Journal of Computational Physics*, 447:110668, 2021.
- [6] Yifan Chen, Houman Owhadi, and Florian Schäfer. Sparse cholesky factorization for solving nonlinear pdes via gaussian processes. *arXiv preprint arXiv:2304.01294*, 2023.
- [7] David Maxwell Chickering. Optimal structure identification with greedy search. *Journal of machine learning research*, 3(Nov):507–554, 2002.
- [8] Matthieu Darcy, Boumediene Hamzi, Giulia Livieri, Houman Owhadi, and Peyman Tavallali. One-shot learning of stochastic differential equations with data adapted kernels. *Physica D: Nonlinear Phenomena*, 444:133583, 2023.
- [9] MIT Critical Data, Justin D Saliccioli, Yves Crutain, Matthieu Komorowski, and Dominic C Marshall. Sensitivity analysis and model validation. *Secondary analysis of electronic health records*, pages 263–271, 2016.

- [10] Paul A Dirmeyer, Pierre Gentine, Michael B Ek, and Gianpaolo Balsamo. Land surface processes relevant to sub-seasonal to seasonal (s2s) prediction. In *Sub-Seasonal to Seasonal Prediction*, pages 165–181. Elsevier, 2019.
- [11] Alireza Doostan and Houman Owhadi. A non-adapted sparse approximation of pdes with stochastic inputs. *Journal of Computational Physics*, 230(8):3015–3034, 2011.
- [12] Mathias Drton and Marloes H Maathuis. Structure learning in graphical modeling. *Annual Review of Statistics and Its Application*, 4:365–393, 2017.
- [13] Jerome Friedman, Trevor Hastie, and Robert Tibshirani. Sparse inverse covariance estimation with the graphical lasso. *Biostatistics*, 9(3):432–441, 2008.
- [14] Jody Hoffer Gittell and Hebatallah Naim Ali. *Relational analytics: Guidelines for analysis and action*. Routledge, 2021.
- [15] Madelyn Glymour, Judea Pearl, and Nicholas P Jewell. *Causal inference in statistics: A primer*. John Wiley & Sons, 2016.
- [16] Boumediene Hamzi, Romit Maulik, and Houman Owhadi. Simple, low-cost and accurate data-driven geophysical forecasting with learned kernels. *Proceedings of the Royal Society A*, 477(2252):20210326, 2021.
- [17] Boumediene Hamzi and Houman Owhadi. Learning dynamical systems from data: A simple cross-validation perspective, part i: Parametric kernel flows. *Physica D: Nonlinear Phenomena*, 421:132817, 2021.
- [18] Boumediene Hamzi, Houman Owhadi, and Yannis Kevrekidis. Learning dynamical systems from data: A simple cross-validation perspective, part iv: case with partial observations. *Physica D: Nonlinear Phenomena*, 454:133853, 2023.
- [19] P Howard. Modeling with ode. *Lecture Notes*, 2009.
- [20] Toru Ishihara. Enumeration of hypergraphs. *European Journal of Combinatorics*, 22(4):503–509, 2001.
- [21] David Lopez-Paz, Krikamol Muandet, Bernhard Schölkopf, and Iliya Tolstikhin. Towards a learning theory of cause-effect inference. In *International Conference on Machine Learning*, pages 1452–1461. PMLR, 2015.
- [22] Charles A Micchelli and Theodore J Rivlin. A survey of optimal recovery. In *Optimal estimation in approximation theory*, pages 1–54. Springer, 1977.
- [23] Sebastian Mika, Bernhard Schölkopf, Alexander J Smola, Klaus-Robert Müller, Matthias Scholz, and Gunnar Rätsch. Kernel pca and de-noising in feature spaces. In *NIPS*, volume 11, pages 536–542, 1998.
- [24] Stephen L Morgan and Christopher Winship. *Counterfactuals and causal inference*. Cambridge University Press, 2015.
- [25] Art B Owen. Variance components and generalized sobol’indices. *SIAM/ASA Journal on Uncertainty Quantification*, 1(1):19–41, 2013.
- [26] H. Owhadi and C. Scovel. *Operator Adapted Wavelets, Fast Solvers, and Numerical Homogenization, from a game theoretic approach to numerical approximation and algorithm design*. Cambridge Monographs on Applied and Computational Mathematics. Cambridge University Press, 2019.
- [27] H. Owhadi, C. Scovel, and F. Schäfer. Statistical Numerical Approximation. *Notices of the AMS*, 66(10), 2019.
- [28] Houman Owhadi. Computational graph completion. *Research in the Mathematical Sciences*, 9(2):1–33, 2022.
- [29] Houman Owhadi. Do ideas have shape? idea registration as the continuous limit of artificial neural networks. *Physica D: Nonlinear Phenomena*, 444:133592, 2023.
- [30] Houman Owhadi, Clint Scovel, and Gene Ryan Yoo. *Kernel Mode Decomposition and the programming of kernels*. Springer, 2021.
- [31] Richard S. Palais. The symmetries of solitons, 1997.
- [32] Jonas Peters, Dominik Janzing, and Bernhard Schölkopf. *Elements of causal inference: foundations and learning algorithms*. The MIT Press, 2017.
- [33] Christopher X Ren, Sidhant Misra, Marc Vuffray, and Andrey Y Lokhov. Learning continuous exponential families beyond gaussian. *arXiv preprint arXiv:2102.09198*, 2021.

- [34] Karen Sachs, Omar Perez, Dana Pe’er, Douglas A Lauffenburger, and Garry P Nolan. Causal protein-signaling networks derived from multiparameter single-cell data. *Science*, 308(5721):523–529, 2005.
- [35] Florian Schäfer, Matthias Katzfuss, and Houman Owhadi. Sparse cholesky factorization by kullback–leibler minimization. *SIAM Journal on Scientific Computing*, 43(3):A2019–A2046, 2021.
- [36] Florian Schäfer and Houman Owhadi. Sparse recovery of elliptic solvers from matrix-vector products. *SIAM Journal on Scientific Computing*, 2023.
- [37] Florian Schäfer, Timothy John Sullivan, and Houman Owhadi. Compression, inversion, and approximate pca of dense kernel matrices at near-linear computational complexity. *Multiscale Modeling & Simulation*, 19(2):688–730, 2021.
- [38] Frank Schweitzer, Giorgio Fagiolo, Didier Sornette, Fernando Vega-Redondo, Alessandro Vespignani, and Douglas R White. Economic networks: The new challenges. *science*, 325(5939):422–425, 2009.
- [39] RAJEN D SHAH and JONAS PETERS. The hardness of conditional independence testing and the generalised covariance measure. *The Annals of Statistics*, 48(3):1514–1538, 2020.
- [40] Ilya M Sobol. Global sensitivity indices for nonlinear mathematical models and their monte carlo estimates. *Mathematics and computers in simulation*, 55(1-3):271–280, 2001.
- [41] IM Sobol’. Sensitivity estimates for nonlinear mathematical models. *Math. Model. Comput. Exp.*, 1:407, 1993.
- [42] Peter Spirtes and Clark Glymour. An algorithm for fast recovery of sparse causal graphs. *Social science computer review*, 9(1):62–72, 1991.
- [43] Oliver Stegle, Dominik Janzing, Kun Zhang, Joris M Mooij, and Bernhard Schölkopf. Probabilistic latent variable models for distinguishing between cause and effect. *Advances in neural information processing systems*, 23, 2010.
- [44] Wenyue Sun, Chuan Tian, and Guang Yang. Network analysis of the stock market, 2015.
- [45] Aldo V Vecchia. Estimation and model identification for continuous spatial processes. *Journal of the Royal Statistical Society Series B: Statistical Methodology*, 50(2):297–312, 1988.
- [46] K Zhang, J Peters, D Janzing, and B Schölkopf. Kernel-based conditional independence test and application in causal discovery. In *27th Conference on Uncertainty in Artificial Intelligence (UAI 2011)*, pages 804–813. AUAI Press, 2011.